On the evolution of an ice shelf melt channel at the base of Filchner Ice Shelf, from observations and viscoelastic modeling

Angelika Humbert[1,2], Julia Christmann[1], Hugh F. J. Corr[3], Veit Helm[1], Lea-Sophie Höyns[1,4],
Coen Hofstede[1], Ralf Müller[5,6], Niklas Neckel[1], Keith W. Nicholls[3], Timm Schultz[5,6], Daniel Steinhage[1],
Michael Wolovick[1], and Ole Zeising[1,2]

[1]Alfred-Wegener-Institut Helmholtz-Zentrum für Polar- und Meeresforschung, Bremerhaven, Germany
[2]University of Bremen, Department of Geosciences, Bremen, Germany
[3]British Antarctic Survey, Natural Environment Research Council, Cambridge, UK
[4]University of Bremen, Department of Mathematics and Computer Science, Bremen, Germany
[5]Institute of Applied Mechanics, University of Kaiserslautern, Kaiserslautern, Germany
[6]Division of Continuum Mechanics, Technical University of Darmstadt, Darmstadt, Germany

Correspondence: Angelika Humbert (angelika.humbert@awi.de)

Abstract. Ice shelves play a key role in the stability of the Antarctic Ice Sheet due to their buttressing effect. A loss of buttressing as a result of increased basal melting or ice shelf disintegration will lead to increased ice discharge. Some ice shelves exhibit channels at the base that are not yet fully understood. In this study, we present in-situ melt rates of a channel which is up to $330\,\mathrm{m}$ high and located at the southern Filchner Ice Shelf. Maximum observed melt rates are $2.3\,\mathrm{m\,a^{-1}}$. Melt

5   rates decline inside the channel along flow and turn into freezing $55\,\mathrm{km}$ downstream of the grounding line. While closer to the grounding line melt rates are higher within the channel than outside, this reverses further downstream. Comparing the evolution of this channel under present-day climate conditions over 250 years with its present geometry reveals a mismatch. This mismatch indicates melt rates two times higher were necessary over the past 250 years to form today's channel geometry. In contrast, forcing the model with present-day melt rates results in a closure of the channel, which contradicts observations.

10   Time series of melt rate measurements show strong tidally-induced variability in vertical strain-rates. We found no evidence of seasonality, but discrete pulses of increased melting occurred throughout the measurement period. The type of melt channel in this study diminishes with distance from the grounding line and are hence not a destabilizing factor for ice shelves.

1   Introduction

Melt channels in ice shelves have been hypothesized to destabilize ice shelves and were often linked to enhanced basal melt.

15   This triggered a variety of observational studies (Le Brocq et al., 2013; Langley et al., 2014; Drews, 2015; Marsh et al., 2016; Dow et al., 2018; Hofstede et al., 2021a). However, such channels diminish with increasing distance from the grounding line at numerous locations. The main questions are thus if such channels are indeed locations of enhanced basal melt and what causes them to diminish.

Channels at the base of ice shelves may either be incised by subglacial channels beneath the inland ice transporting water

20   into the ocean (Le Brocq et al., 2013), arise from topographic features or from shear margins developing surface troughs when

adjusting to floatation (Alley et al., 2019). Such features like bedrock undulations or eskers imprinted into the ice geometry on the inland ice side create a channel-type geometry on the floating part (Drews et al., 2017; Jeofry et al., 2018). In both cases, the channel at the ice base will be altered by two factors: basal melt arising from oceanic heat and viscoelastic creep. Surface troughs on ice shelves, which are detectable by satellites- and airborne remote sensing, are linked due to buoyancy
25 equilibrium to incisions at the ice base, thus either to melt channels (e.g. Le Brocq et al., 2013; Langley et al., 2014) or to basal crevasses (e.g. Humbert et al., 2015). Channels at the ice base have been surveyed using radio echo sounding (Rignot and Steffen, 2008; Vaughan et al., 2012; Le Brocq et al., 2013; Dutrieux et al., 2014; Langley et al., 2014; Dow et al., 2018). The typical dimensions range from $300 - 500\,\mathrm{m}$ wide and up to $50\,\mathrm{m}$ high channels (Langley et al., 2014) to $1 - 3\,\mathrm{km}$ wide and $200 - 400\,\mathrm{m}$ high ones (Rignot and Steffen, 2008). Channel flanks are not necessarily smooth but may form terrace structures
30 in lateral (across ice flow) dimension as shown by Dutrieux et al. (2014) for Pine Island Glacier, Antarctica. These terraces are separated by up to $50\,\mathrm{m}$ high walls with steep slopes between $40°$ and $60°$.

Hofstede et al. (2021a) found a basal channel on Support Force Glacier at the transition to Filchner Ice Shelf attributed to the outflow of subglacial water. The channel increases in height close to the grounding line and widens afterwards. Between 7 and $14\,\mathrm{km}$ from the grounding line, the flanks of the channel became steeper and terraces formed on its sides, which are
35 sustained over $38\,\mathrm{km}$ from the grounding line, but decline in height between 14–$38\,\mathrm{km}$. Within this distance, the height varied only slightly from 170 to $205\,\mathrm{m}$. This particular channel is the focus of this study.

In-situ observations of melt rates in such channels are often conducted with a phase sensitive Radio Echo Sounder (pRES), which is described in more detail below. Basal melt rates in a channel at Ross Ice Shelf, Antarctica were found by Marsh et al. (2016) to be up to $22.2\,\mathrm{m\,a^{-1}}$ near the grounding line and only $2.5\,\mathrm{m\,a^{-1}}$ for observations $40\,\mathrm{km}$ downstream. In lateral
40 direction, the melt rate is only $0.82\,\mathrm{m\,a^{-1}}$ demonstrating enhanced melt inside the channel. At Pine Island Glacier, Antarctica, Stanton et al. (2013) found basal melt rates of up to $24\,\mathrm{m\,a^{-1}}$ and an across-channel variability that they suggested to be related to channelized flow. The decreasing of melt rates inside the channel in the flow direction is likewise described by Le Brocq et al. (2013). Uprising fresh water enhances basal melting inside the channel. At some point, it becomes super-cooled due to the falling pressure. Thus, the melt rate decreases and could even change to refreezing. Similar to Le Brocq et al. (2013),
45 Marsh et al. (2016) assumed that the channel at Ross Ice Shelf is formed by the outflow of subglacial meltwater. Washam et al. (2019) found high seasonal variability in basal melting within a channel at Petermann Gletscher, Greenland. In summer, melt rates reached a maximum of $80\,\mathrm{m\,a^{-1}}$, whereas in winter, melt rates were below $5\,\mathrm{m\,a^{-1}}$. They suggested that increased subglacial discharge during summer strengthens ocean currents under the ice which drives the high melt rates. Besides seasonal variability, melt rates also change within smaller periods. Vaňková et al. (2020) identified melt rate variations at the $\mathrm{M_2}$ tidal
50 constituent at six of 17 locations at Filchner-Ronne Ice Shelf, Antarctica.

Modeling basal melt rates requires coupled ice-ocean models, solving the energy jump condition at the transition of ice to the ocean. While none of the global circulation models deals with ice shelf cavities, there are some coupled ice-sheet-ocean models simulating large scale basal melt rates (Gwyther et al., 2020; Dinniman et al., 2016; Jourdain et al., 2017; Seroussi et al., 2017; Timmermann and Hellmer, 2013; Galton-Fenzi et al., 2012). However, only a few of them incorporate melt channels: Gladish
55 et al. (2012) showed that channels confine the warm water and stabilize the ice shelf by preventing melt on broader spatial

scales. This conclusion is affirmed by Millgate et al. (2013) who found that an increasing number of melt channels lead to a decreasing overall mean melt rate. Our study will provide an observational dataset of basal melt rates that allows assessing this type of modeling.

The change in geometry due to mechanical deformation is another important contribution to the evolution of basal channels.
60 The gradients in displacement u lead to strain ε that causes a change in ice thickness. This component is governed by the viscoelastic nature of a Maxwell fluid for ice. While ice is reacting purely viscous on long time scales, its behavior on short time scales is elastic (Reeh et al., 2000; Gudmundsson, 2011; Sergienko, 2013; Humbert et al., 2015; Christmann et al., 2016; Schultz, 2017; Christmann et al., 2019). The transition from grounded to floating ice and short term geometry changes due to basal melt or accumulation are examples of ice affected by the elastic response. Over time scales of years, viscous creep
65 becomes more relevant. As a consequence, the geometry of melt channels needs to be modeled using viscoelastic material models, which we will also engage below.

In this study, we present in-situ melt rates of a large melt channel feature of the southern Filchner Ice Shelf at the inflow from Support Force Glacier (SFG). Field measurement and satellite-borne data enable us to investigate how this feature evolves using numerical modeling. In addition to the spatial distribution of basal melt, we are analyzing the temporal evolution of melt
70 rates. We split this manuscript into two main parts, starting with observations followed by a modeling section. We present the methodology and the results in each part separately. A synthesis is then focusing on the evolution of the melt channel.

2 Observations

2.1 Data acquisition

We acquired data at a melt channel on the southern Filchner Ice Shelf under the framework of the Filchner Ice Shelf Project
75 (FISP). We performed 44 phase-sensitive radar (pRES) measurements (locations are shown in Fig. 1) in the season 2015/16, that have been repeated in 2016/17 as Lagrangian-type measurements. These measurements were taken in 13 cross-sections ranging from 14 to $61\,\mathrm{km}$ downstream the grounding line (Fig. 1). This allows us to investigate the spatial variability of basal melt rates. At each cross-section, up to four measurements were performed at different locations: at the steepest western flank (SW), at the lowest surface elevation (L), at the steepest eastern flank (SE) and outside east of the channel (OE; Fig. 1b). In order
80 to achieve an all-year time series, one autonomous pRES (ApRES) station was installed (Fig. 1b). This instrument performed autonomous measurements every two hours resulting in 4342 measurements between 10 January 2017 and 6 January 2018. A GPS station was also in operation at this point from December 24, 2015 to May 5, 2016. To distinguish the single-repeated measurements from the autonomous measurements, we refer to them as *pRES* and *ApRES* measurements.
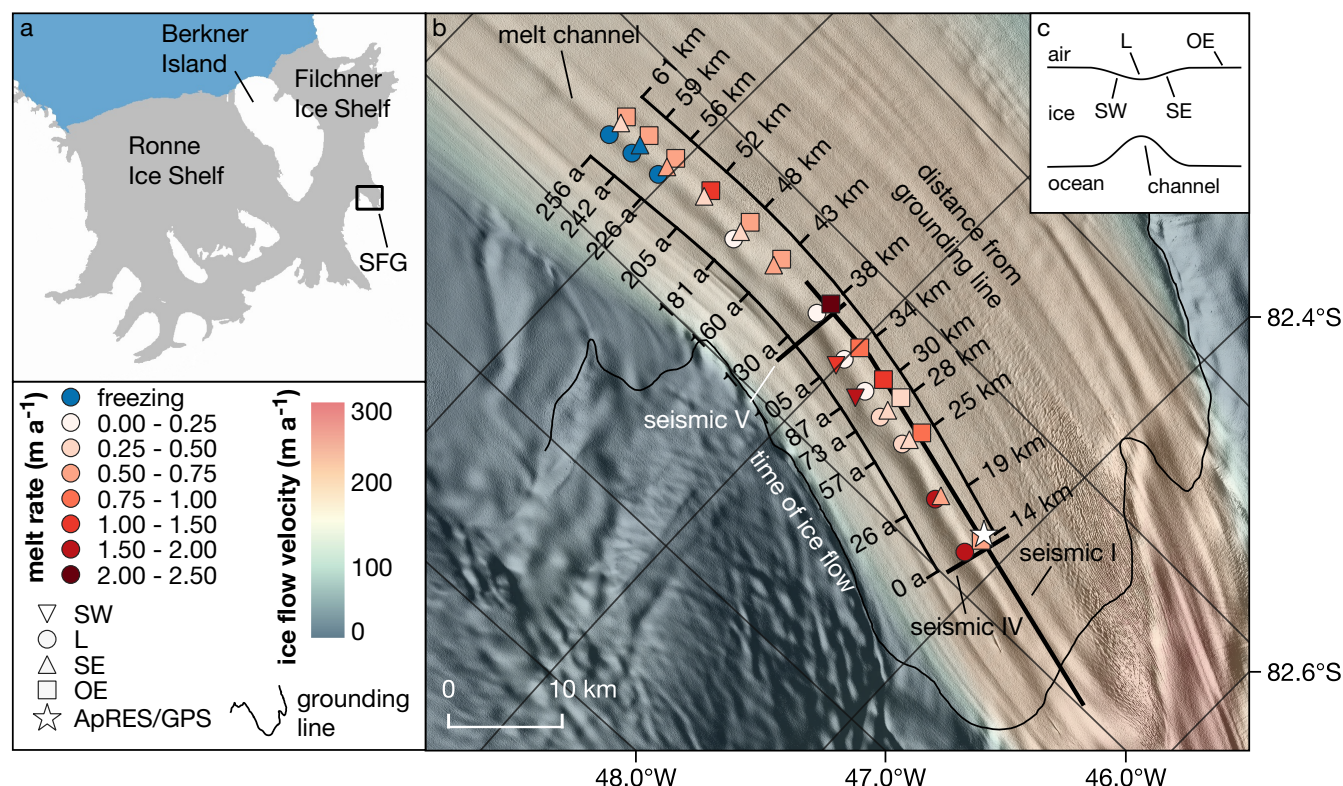
Figure 1. (a) Map of the Ronne and Filchner ice shelves (BedMachine Antarctica (Morlighem, 2020; Morlighem et al., 2020)). The study area near the Support Force Glacier (SFG) is marked with a black box. (b) Study area with pRES-derived basal melt rates at 13 cross-sections of the melt channel. The different symbols indicate the position relative to the channel, as shown in (c). For each cross-section, the distance from the grounding line and the duration of ice flow from the location furthest upstream are given. The location of an ApRES/GPS station is shown by a star. The seismic I, IV and V lines mark the location of active seismic profiles (Hofstede et al., 2021a, b). The background is a hillshade of the Reference Elevation Model of Antarctica (Howat et al., 2018, 2019) overlaid by the ice flow velocity (Hofstede et al., 2021a). (c) Sketch of a cross-section of the channel with measurement locations on the steepest western surface flank (SW), at the lowest surface elevation (L), on the steepest eastern surface flank (SE) and outside east of the channel (OE).

2.2 Materials and methods

2.2.1 pRES device and processing

The pRES device is a low-power, ground-based radar that allows for estimating displacement of layers from repeated measurements with a precision of millimeters (Brennan et al., 2014). This accuracy enables investigating even small basal melt rates, taking snow accumulation together with firn compaction and strain in vertical direction into account (Corr et al., 2002; Jenkins et al., 2006). The pRES is a frequency modulated continuous wave (FMCW) radar that transmits a sweep, called *chirp*, over a period of one second with a center frequency of 300 MHz and bandwidth of 200 MHz (Nicholls et al., 2015). For a better signal

to noise ratio, the single-repeated measurements were performed with 100 chirps per measurement and the measurements of the time series with 20 chirps due to memory and power limitations. After collecting the data, each chirp was correlated with every other chirp in order to reject those which had a low correlation coefficient on average. The remaining chirps were stacked.

We followed Brennan et al. (2014) and Stewart et al. (2019) for data processing to get amplitude- and phase-depth profiles.
95 The final profile that contains the amplitude and phase information as a function of two-way travel time was received from a Fourier transformation. To convert two-way travel time into depth, the propagation velocity of the radar wave is computed following Kovacs et al. (1995). For this the density is required. Here we use a model described by Herron and Langway (1980). As input parameters, accumulation rate and mean annual temperature is needed, for which we use data from the regional climate model RACMO 2.3/ANT (van Wessem et al., 2014, multi-annual mean 1979 – 2011). Despite the correction of higher
100 propagation velocities in the firn, the uncertainty of the velocity and thus of the depth is 1% (Fujita et al., 2000).

2.2.2 Basal melt rates from repeated pRES measurements

The method for determining basal melting rates, previously described by e.g. Nicholls et al. (2015) and Stewart et al. (2019), is based on the ice thickness evolution equation. The change in ice thickness over time $\partial H/\partial t$ consists of a component arising from deformation and accumulation/ablation at both interfaces (e.g. Zeising and Humbert, 2021). As our observations are
105 discrete in time, the change of ice shelf thickness ΔH within the time period Δt, that is caused by changes at the surface and in the firn ΔH_s (e.g. snow accumulation/ablation and firn compaction), by strain in vertical direction ΔH_ε and by thickness changes due to basal melt ΔH_b is considered:

$$\frac{\Delta H}{\Delta t} = \frac{\Delta H_s}{\Delta t} + \frac{\Delta H_\varepsilon}{\Delta t} + \frac{\Delta H_b}{\Delta t} \tag{1}$$

(Vaňková et al., 2020; Zeising and Humbert, 2021). In order to obtain the basal melt rate, the change in ice thickness must be adjusted for the other contributions. Snow accumulation/ablation, firn compaction but also changes in radar hardware (and
110 settings) can cause an vertical offset near the surface that cannot be distinguished from one another. Following Jenkins et al. (2006), we aligned both measurements below the firn-ice transition. To this end, we compute the depth of pore closure h_{pc} takes place, i.e. the depth at which a density of $830\,\mathrm{kg\,m^{-3}}$ is reached. To this end, we apply the densification model (Herron and Langway, 1980) and mean annual accumulation rate and temperature from the multi-year mean RACMO2.3 product (van Wessem et al., 2014). In our study area, h_{pc} varies between $62\,\mathrm{m}$ and $71\,\mathrm{m}$. The actual alignment is based on a correlation of
115 the amplitudes for a window of $6\,\mathrm{m}$ around h_{pc}. No reliable alignment could be obtained from the correlation for nine stations, since the correlation values were ~~not~~ unambiguous. As a consequence, these stations were not considered.

After the alignment, the change in the ice thickness H_i below the depth of the pore close h_{pc} is only affected by vertical strain and basal melt. Thus the basal melt rate a_b (positive for melting, negative for freezing) is

$$a_b = -\frac{\Delta H_b}{\Delta t} = -\left(\frac{\Delta H_i}{\Delta t} - \frac{\Delta H_\varepsilon}{\Delta t}\right) \tag{2}$$

with ΔH_ε being the thickness change due to vertical strain ε_{zz}. ΔH_ε is derived from integrating ε_{zz} from the aligned reflector
120   at h_{pc} to the ice base h_b

$$\Delta H_\varepsilon = \int_{\overline{h_b}}^{h_{\mathrm{pc}}} \varepsilon_{\mathrm{zz}}\, \mathrm{d}z. \tag{3}$$

Here, $\overline{h_b}$ denotes the averaged depth of the ice base of the measurements. The vertical strain is defined as

$$\varepsilon_{zz} = \frac{\partial u_z}{\partial z} \tag{4}$$

with the displacement in vertical direction u_z.

In order to determine u_z, we followed the method described by Stewart et al. (2019). We divided the first measurement in
segments of $6\,\mathrm{m}$ width with $3\,\mathrm{m}$ overlap from a depth of $20\,\mathrm{m}$ below the surface to $20\,\mathrm{m}$ above the ice base. To determine
125   vertical displacements, we cross-correlated each segment of the first measurement with the repeated measurement. The lag of
the largest amplitude correlation coefficient was used to find the correct minimum phase difference, from which we derived
the vertical displacement. Since noise prevents the reliable estimation of the vertical displacement from a certain depth on, we
calculated the depth at which the averaged correlation of unstacked chirps undercuts the empirical value of 0.65. We name this
the noise-level depth limit h_{nl}, which is $743\,\mathrm{m}$ on average in this study area. Only those segments located below h_{pc} and above
130   h_{nl} were used to avoid densification processes and noise to influence the strain estimation. A linear regression was calculated
from the shifts of the remaining segments, assuming a constant vertical strain distribution over depth as the overall trend.
However, at six stations, all in the hinge zone where the ice is bended by tides, we observed a slight deviation from a linear
trend at deeper layers (Fig. A1a). The segments that indicate a non-linear distribution are located below h_{nl} and are hence not
taken into account for the regression. Nevertheless, we want to provide a lower limit considering other forms of strain-depth
135   relations. For this purpose, we use a strain model that is decreasing linearly from half the ice thickness (approximately h_{nl}) to
the depth of at which $\varepsilon_{zz} = 0$ (Fig. A1b). This serves as a lower limit of the displacement, whereas a linear $\varepsilon_{zz}(z)$ gives the
upper limit. The average of both gives ΔH_ε and the difference the uncertainty.

In order to derive ΔH_i, we used a wider segment of $10\,\mathrm{m}$ around the basal return, which was identified by a strong increase
in amplitude. Its upper limit is located $9\,\mathrm{m}$ above the basal return, while the lower limit is defined $1\,\mathrm{m}$ below the basal return.
140   The vertical displacement of the ice base and thus the change in ice thickness was obtained from the cross-correlation of the
basal segment.

The uncertainty of the melt rate results mainly from the alignment of the repeated measurement and the uncertainty of ΔH_ε.
This leads to uncertainties in the melt rate of more than $0.2\,\mathrm{m\,a}^{-1}$ for locations in the hinge zone, while at other locations the
uncertainty is predominantly in the range of $< 0.05\,\mathrm{m\,a}^{-1}$.
145   In order to classify how representative the melt rates are for the past, we reconstructed the ice thickness based on the values
derived from the pRES measurements. First, we interpolated the a_b, ΔH_ε and ΔH_s along the distance of the channel to get
continuous values between the cross-sections and smoothed the results in order to obtain a trend for each process. We converted
the distance downstream of the ~~the~~ upstream most cross-section to an age beyond this cross-section by assuming the mean flow

velocity is constant. Next, we treat the change in ice thickness as a transport equation. To this end, we compute the advection of

150 the ice thickness under present day climate conditions (H_{PDadv}). For this we use interpolated functions of $a_b(t)$, $\Delta H_\varepsilon(t)$ and $\Delta H_s(t)$. The expected ice thickness at H_{PDadv} is then the thickness at $t_0 = 0\,\mathrm{a}$ plus the cumulative change in ice thickness:

$$H_{\mathrm{PDadv}}(t) = H(t_0) + \int_{t_0}^{t} \left(\Delta H_s(t') + \Delta H_\varepsilon(t') + a_b(t') \right) dt'. \tag{5}$$

We can turn this around and calculate a synthetic melt rate $a_b^{\mathrm{syn}}(t)$ that reconstructs the ice thickness H:

$$H(t) = H(t_0) + \int_{t_0}^{t} \left(\Delta H_s(t') + \Delta H_\varepsilon(t') + a_b^{\mathrm{syn}}(t') \right) dt'. \tag{6}$$

Descriptions of the symbols are given in Tab. A1.

2.2.3 Basal melting from ApRES time series

155 The processing of the autonomous measured time series differs slightly from the single-repeated measurements. For the ApRES time series, the instrument was located below the surface, thus snow accumulation had no influence on the measured ice thickness and an alignment of the measurements is not necessary. This gives the possibility to determine the firn compaction ΔH_f. Without the alignment, thickness change due to strain needs to be considered for the whole ice thickness H

$$\Delta H_\varepsilon = \int_{0}^{H} \varepsilon_{zz}\,\mathrm{d}z. \tag{7}$$

For processing, we followed the method described by Zeising and Humbert (2021), which differs slightly from the processing

160 applied by Vaňková et al. (2020). Similar to processing of the single-repeated measurements, we divided the first measurement into the same segments and calculated the cross-correlation of the first measurement (t_1) with each repeated measurement (t_i). The displacement was obtained by the lag of the minimum phase difference. To avoid half-wavelength ambiguity due to phase wrapping, we limited the range of expected lag based on the displacement derived for the period $t_1 - t_{i-1}$.

The estimation of the vertical strain for the period $t_1 - t_i$ is based on a regression analysis of the vertical displacements for

165 chosen segments. Only those segments located below a depth of $70\,\mathrm{m}$ and above the noise-level depth limit of $h \approx 600\,\mathrm{m}$ were used to avoid densification processes and noise to influence the strain estimation. Assuming constant strain over depth (which is a first guess only), the regression analysis gives the vertical strain and the cumulative displacement $u_z(z)$ is

$$u_z(z) = \varepsilon_{zz}\,z + \Delta H_f \tag{8}$$

where the intercept at the surface is the firn compaction ΔH_f. By increasing the time period, the cumulative melt of the ApRES time series is derived.

170 In order to investigate if the basal melt is affected by tides, we first de-trended the cumulative melt time series and computed the frequency spectrum afterwards. Subsequently, we used frequencies up to the solar annual constituent as input for a harmonic

fit of $\Delta H(t)$. We then de-tided $\Delta H(t)$ by subtracting the harmonic fit and calculated the thinning rate. Assuming, that basal melt causes changes on short time scales of several days, we attribute abrupt increases in the thinning rate to basal melt anomalies.

175 ### 2.2.4 Global Positioning System (GPS) processing

The GPS processing is similar to the method used by Christmann et al. (2021). With the Waypoint GravNav 8.8 processing software, we applied a kinematic precise point positioning (PPP) processing for the GPS data that were stored in daily files. We merged three successive daily solutions to enable full day overlaps avoiding jumps between individual files. Afterwards, we combined the files in the middle of each 1-day overlap using relative point to point distances and removed outliers. The
180 data has been low-pass filtered for frequencies higher than $1/3600\,\mathrm{Hz}$. For tidal analysis, we calculated the power spectrum of the vertical displacement.

2.2.5 Digital Elevation Model (DEM)

We use the TanDEM-X PolarDEM 90m Digital Elevation data product provided by the German Aerospace Center (DLR) as reference elevation model (DLR, 2020). As the elevation values represent ellipsoidal heights relative to the WGS84 ellipsoid
185 we refer the PolarDEM to the EIGEN-6C4 Geoid (Foerste et al., 2014). In the following, we refer the DEM heights above Geoid as observed surface elevation h_{TDX}. The absolute vertical height accuracy of the PolarDEM is validated against ICESat data and given to be $< 10\,\mathrm{m}$ (Rizzoli et al., 2017). For our region of interest the accuracy is given to be $< 5\,\mathrm{m}$ as shown in Fig. 16 of Rizzoli et al. (2017).

2.3 Results and discussion of observations

190 #### 2.3.1 Spatial melt rate distribution around basal channel

The estimated basal melt rates derived from single-repeated pRES measurements range from 0 to $2.3\,\mathrm{m\,a^{-1}}$ (Fig. 2a). Some stations indicate basal freezing. A trend of decreasing melt rates in along channel direction was found at the thinnest part (L) of the channel. Here, melt rates decrease from $1.8\,\mathrm{m\,a^{-1}}$ to basal freezing, measured at the three most downstream cross-sections. Outside of the channel (OE), basal melt rates are more variable without a trend. Stations at the eastern flank (SE) show a lower
195 range. Here, a_b varies between basal freezing and $0.8\,\mathrm{m\,a^{-1}}$.

The height of the channel (difference in ice thickness between L and OE; Fig. 2b) increases from about $200\,\mathrm{m}$ at the southernmost cross-section to a maximum difference of about $330\,\mathrm{m}$ over a distance of $20\,\mathrm{km}$ in ice flow direction. At this location the melt rates within the channel fall below those outside the channel and the height of the channel decreases, reaching $\sim 100\,\mathrm{m}$
200 at the northernmost cross-section.

In Fig. 2c we display the melt rates as a function of ice-shelf draft, derived from the TanDEM-X surface elevation and the pRES ice thickness. The melt rates outside the channel (OE) seem to be independent of the ice-shelf draft, while inside the

channel (L) the melt rates decrease with reduced draft. However, melt rates at the largest drift inside the channel are approx.
three times larger than those outside the channel or at the steepest eastern flank (SE) at similar draft.

205   The distribution of ΔH_ε shows a significant thickening of more than $1\,\mathrm{m\,a^{-1}}$ at the most upstream cross-section at L and OE
(Fig. A2). In ice flow direction, ΔH_ε declines, reaching about zero above the channel at the cross-section furthest downstream.
In contrast, outside the channel, strain-thinning occurred $30\,\mathrm{km}$ from the grounding line on. The change in ice thickness due to
firn compaction and accumulation is close to zero in the entire study area (Fig. A2).
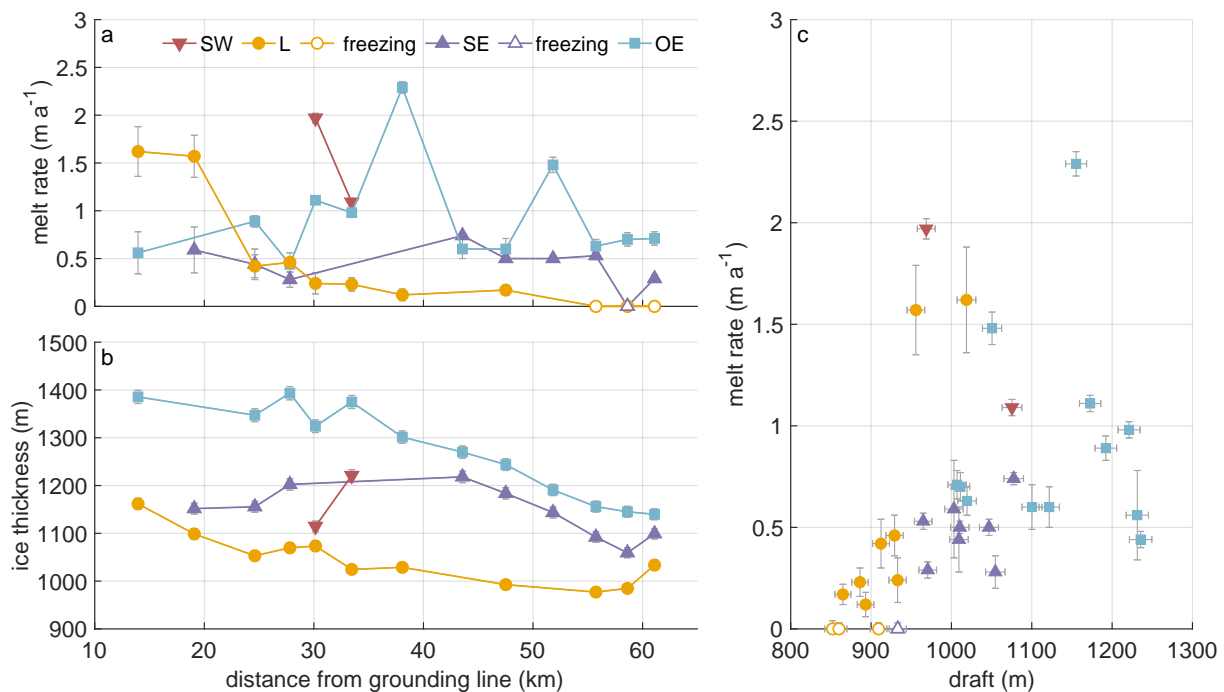
Figure 2. Spatial distribution of pRES-derived (a) basal melt rates (positive a_b represents melting) and (b) ice thickness at the locations SW
(red), L (yellow), SE (purple) and OE (blue) around the channel as a function of distance from the grounding line. (c) Melt rate as a function
of ice draft obtained from pRES-derived ice thickness and h_{TDX}. Uncertainties are shown by gray error bars.

However, the measurements only show a snapshot, as the variability on longer time scales is unknown. Based on the interpo-
210   lated melt rates, ΔH_ε and ΔH_s along the channel (solid lines in Fig. 3a and A2), we computed the advected ice thickness under
present day climate conditions H_{PDadv} (solid lines in Fig. 3b). The comparison of H_{PDadv} with the measured ice thickness
(dashed lines) shows large differences of up to $185\,\mathrm{m}$ above the channel. While the observed ice thickness decreases rapidly
above the channel, H_{PDadv} remains almost constant. In contrast, no significant differences between the observed ice thickness
and H_{PDadv} can be identified outside the channel. If the present day melt rates were representative for a longer period of
215   time, the channel would be closed within 250 years, as the difference in H_{PDadv} above and outside the channel reaches zero.
However, since the channel still exists beyond the northern end of our study area, it can be concluded that the melt rates in

the channel must have been higher in the past. How large the melt rates must have been on average can be deduced from the reconstruction of the existing ice thickness. The resulting synthetic average melt rate in the channel is about twice as high as the observed ones, reaching $3.5\,\mathrm{m\,a^{-1}}$ in the upstream area (yellow dashed line in Fig. 3a). Assuming a steady state ice thickness

220 upstream of the study area (supported by low elevation change found in (Helm et al., 2014)) and constant vertical strain and accumulation in the past, this indicates that melt rates in the last 250 years have been significantly higher than observed now.

In addition to the observations we have presented in this section, we also conducted measurements of the vertical profile of the vertical displacement, that we present below together with simulations.
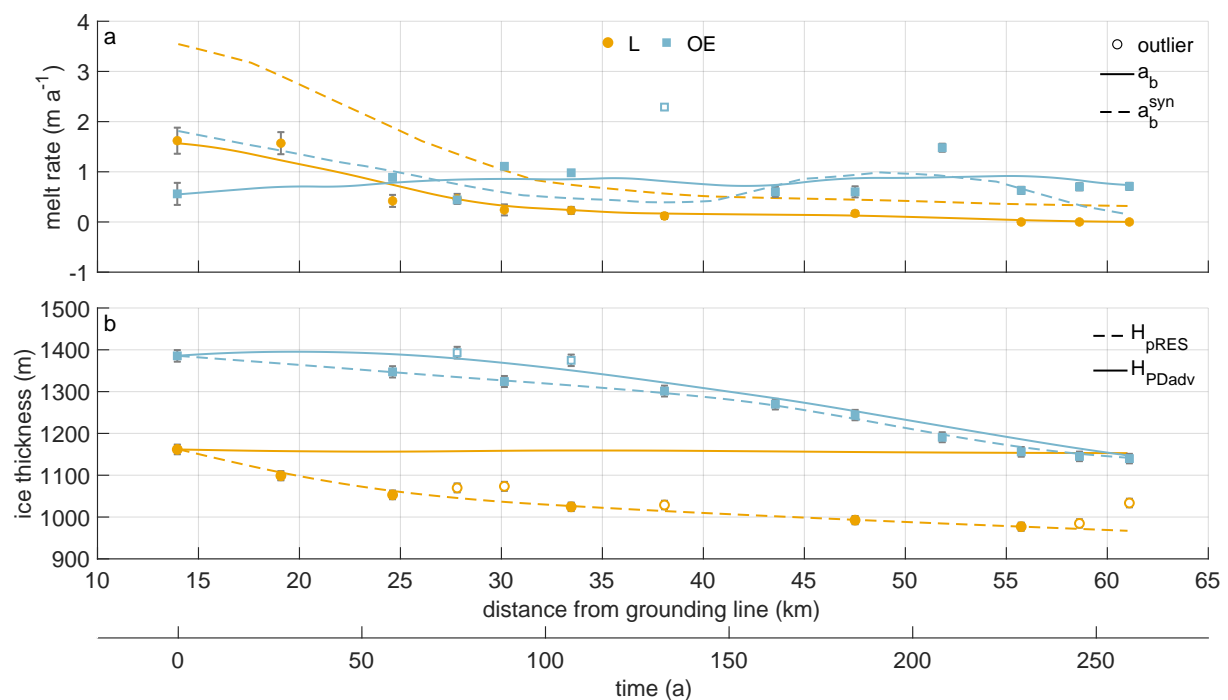
Figure 3. (a) Melt rates at locations L (yellow) and OE (blue) are shown by dots (L) and squares (OE). The interpolated melt rates (a_b) are shown by solid lines and synthetic melt rates (a_b^{syn}) that are necessary to reproduce H_{pRES} at L and OE are shown by dashed lines. (b) Ice thickness at locations L (yellow) and OE (blue) are shown by dots (L) and squares (OE). The interpolated ice thicknesses (H_{pRES}) are shown by dashed lines and the advected ice thicknesses under present day climate conditions (H_{PDadv}) from the observed melt rates at L and OE are shown by solid lines. The two x-axes show the distance from the grounding line in kilometers and the duration of ice flow in years from the measurement location furthest upstream. Unconsidered observations were marked as outliers. Error bars mark the uncertainties of the pRES-derived values.

2.3.2 Time series of basal melting

225 The ApRES time series outside the melt channel reveals an average melt rate of $0.23\,\mathrm{m\,a}^{-1}$ (Fig. 4a). A look at the monthly mean melt rates shows increased melt during the summer months (January, February and November, December) in comparison with the winter season. In these months the melt rates show values from more than $0.3\,\mathrm{m\,a}^{-1}$ up to $0.62\,\mathrm{m\,a}^{-1}$. The unfiltered time series of the cumulative melt shows a tidal signal with amplitudes of $\sim 1\,\mathrm{cm}$ within $12\,\mathrm{h}$ around the low-pass filtered cumulative melt. The spectral analysis shows all main diurnal and semi-diurnal constituents, which is in accordance to the

230 frequencies observed from the GPS station (Fig. A3). The analysis of melt events from the de-tided thinning rate shows several melt anomalies distributed over the entire measurement period (Fig. 4a). These events lasted from a several hours to a few days and melted up to $1.5\,\mathrm{cm}$ of ice.
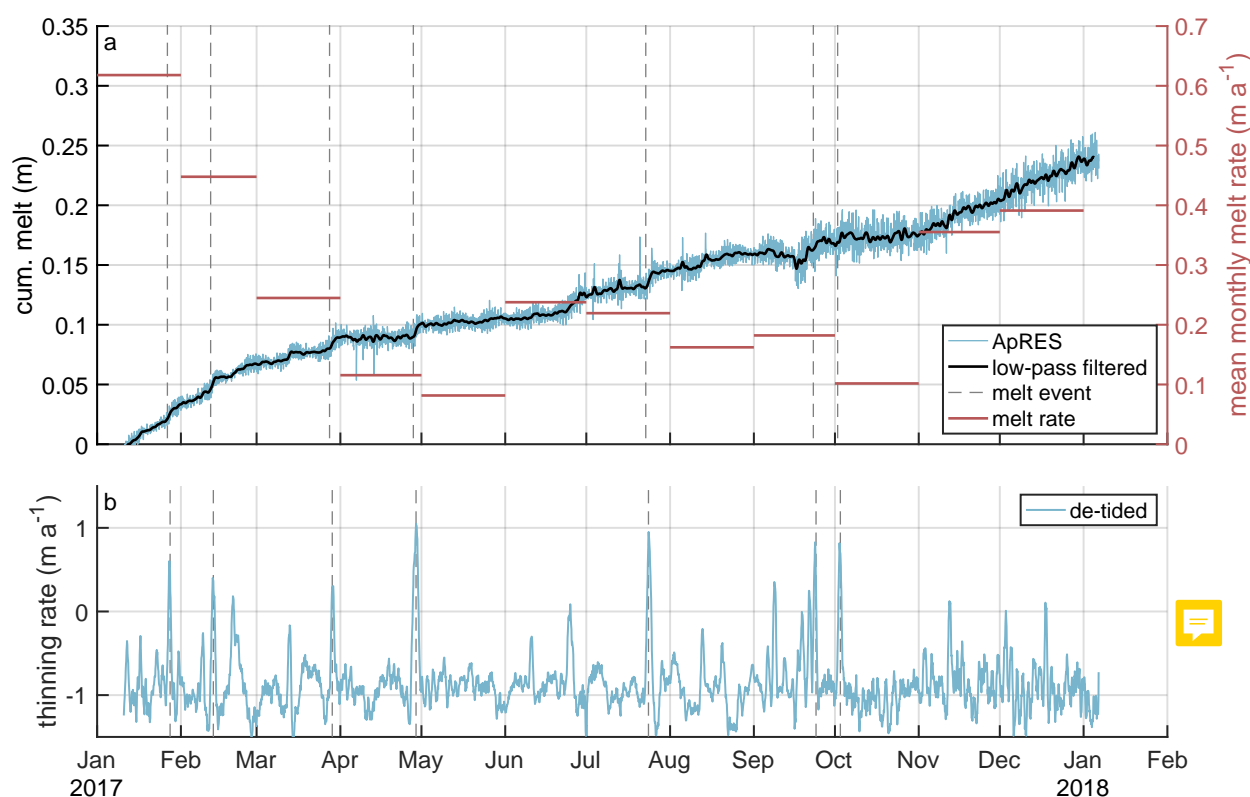
Figure 4. Time series of basal melting at ApRES location outside the channel. (a) Cumulative melt (blue line, left y-axis) over measurement period from 10 January 2017 to 6 January 2018 with low-pass filtered time series (black line). Monthly mean melt rates are shown by red lines on the right y-axis. (b) Thinning rate after subtracting of the tidal signal (blue line). The dashed gray lines in (a) and (b) mark stronger melt events.

We found evidence for a clear accordance of the strain in the upper ice column with the tidal signal as recorded by GPS measurements. Unfortunately, we are lacking vertical strain in the lower column of the ice due to the noise, which permits to
235   extract the temporal variation of basal melt rates on tidal time scales. As the tidal variation of $\Delta H/\Delta t$ is by far lower than the observed $\Delta H_\varepsilon/\Delta t$, either deformation in the upper and lower parts compensates each other or basal melt/freeze takes this role. We can exclude freezing, as we do not find jumps in the amplitude of the basal return in the ApRES signal (Vaňková et al., 2021) over tidal time scales. Consequently, we infer that strain in the lower part compensates the one in the upper part and there is only a small variation of basal melt on tidal time scales.

240   As our location is close to two hinge zones, upstream and west of the melt channel, only a full three-dimensional model could shade light into the vertical strain in the lower part of the ice column. This is numerically costly for the required non-linear strain theory and not in reach. With melt channels being located (or initiated) in the hinge zone, any kind of ApRES time series performed at ice columns with a thickness of more than $1000\,\mathrm{m}$ is affected by the unclear strain-depth profile in the lower part of the ice column. This may be overcome by a radar device with higher transmission power, that allows to detect the vertical
245   displacement of layers down to the base. The observed tidal dependency of the vertical strain is consistent to the finding from other ApRES locations at the Filchner-Ronne Ice Shelf by Vaňková et al. (2020). They found the strongest dependency, even of the basal melt rate at some stations, on the semidiurnal (M_2) constituent. Beside depth-independent tidal vertical strain, (Vaňková et al., 2020) found tidal deformation from elastic bending at ApRES stations located near grounded ice.

3   Viscoelastic modeling

250   To obtain a more profound understanding of the evolution of the channel, we conduct transient simulations and analyze the change in geometry of a 2D cross-sections over time, as well as the simulated strain-field. The simulations are forced with the basal melt rates (both interpolated and synthetic) obtained in this study (Fig. 3). We transform distance to time in along flow direction of the ice shelf (Fig. 1) using present day velocities. This enables us to study under which conditions the channel is stable or vanishes.

255   Ideally, we would have observations of ice geometry and basal melt rates from the transition from inland onward, but our first cross-section with observations is located $14\,\mathrm{km}$ downstream of the grounding line (Fig. 1). The initial elastic response of the grounded ice becoming afloat had faded away. Further elastic contributions to the deformation originates from in-situ melt at the base and accumulation at the surface. To initialize our simulations adequately, we therefore conduct a spin-up.

3.1   Model

260   The model comprises non-linear strain theory accounting for finite deformations, as there is no justification to expect a priori the deformation to be small for simulation times ~~of more~~ than $200\,\mathrm{a}$ (e.g. Haupt, 2002). We treat the ice as a viscoelastic fluid and solve the system of equations for displacements using the commercial finite element software COMSOL (Christmann et al., 2019). The constitutive relation corresponds to a Maxwell material with an elastic response on short time scales and viscous response on long time scales. For homogeneous, isotropic ice, two elastic material parameters exist (Young's modulus

265 and Poisson's ratio). We conduct all viscoelastic simulations with commonly used values for ice for Young's modulus of
1 GPa and Poisson's ratio of 0.325 (Christmann et al., 2019). Another material parameter of the viscoelastic Maxwell material
is the viscosity. It controls the viscous flow of ice. We use a constant viscosity of $5 \times 10^{15}\,\mathrm{Pa\,s}$ and discuss the influence
of this material parameter later on. This constant viscosity is at the upper limit of the viscosity distribution derived by an
inversion of the rate factor in the floating part of Filchner-Ronne Ice Shelf (Appendix Sec. B1 and Fig. B1). This inversion

270 has been conducted using the Ice Sheet and Sea-Level System Model (ISSM) (Larour et al., 2012) in higher-order Blatter-
Pattyn approximation (Blatter, 1995; Pattyn, 2003), BedMachine geometry (Morlighem et al., 2020) and the velocity field of
(Mouginot et al., 2019b, a). It was further supported by a temperature field presented in (Eisen et al., 2020), based on the
geothermal heat flux of (Martos et al., 2017).

The model geometry represents a cross-section through the melt channel (Fig. 5) with the x-direction being across channel

275 and resembling the seismic IV profile (Fig. 1). By assuming plane strain, it is virtually infinite in the y-direction. The com-
putational domain is discretized by an unstructured mesh using prisms with a triangular basis involving a refined resolution
near the channel. We use the direct MUMPS solver and backward differentiation formula with automatic time step control and
quadratic Lagrange polynomials as shape functions for the displacements. The viscous strain is an additional internal variable
in the Maxwell model and we use shape functions of linear discontinuous Lagrange type to save computational effort. In some

280 cases, the geometry evolution leads to degraded mesh elements, which requires automated remeshing from time to time.

In this study, the ice density is $910\,\mathrm{kg\,m^{-3}}$ and the seawater density is $1028\,\mathrm{kg\,m^{-3}}$. At the upper and lower boundaries, we
apply stress boundary conditions: for the ice-ocean interface, a traction boundary condition specifies the water pressure by a
Robin-type condition. The ice-atmosphere interface is traction-free. Laterally, we apply displacement boundary conditions. As
we take a plane strain approach, we can neglect deformation in the downstream direction. To obtain reasonable lateral bound-

285 ary conditions, we transfer observed vertical strain and hence, vertical displacements, in horizontal displacements assuming
incompressibility

$$\varepsilon_{zz} = -(\varepsilon_{xx} + \varepsilon_{yy}), \tag{9}$$

so that u_x becomes

$$u_x = \frac{(\varepsilon_{xx} + \varepsilon_{yy})\,W}{2}. \tag{10}$$

with W the width of the simulated cross-section (Fig. 5). We assume that the horizontal displacements are constant in vertical
direction at lateral boundaries, resulting in a compression or elongation perpendicular to the channel (Fig. B2a).

290 The climate forcing consists of the SMB and basal melt rate. Technically, both are applied by changing the geometry of
the reference configuration with the respective cumulative quantities (Fig. B2b,c). For the SMB, we used multi-year mean
RACMO2.3 data (van Wessem et al., 2014) ranging from 0.15 to $0.17\,\mathrm{m\,a^{-1}}$ for a density of $910\,\mathrm{kg\,m^{-3}}$, that we slightly
modified to account for the surface depression over the channel: accumulation measurements at the pRES locations indicated
higher accumulation in the channel than outside by a factor of roughly 1.5. Thus, we used 50% higher accumulation rates above

295 the basal channel and a smooth cosine-shaped transition in x-direction. A crucial forcing is of course the basal melt rate. Here

we conduct individual experiments that are based on our observed melt rates and its variations. As this data is spatially sparse, we need to interpolate those values in across-channel (x) direction. To this end, we assume a smooth cosine-shaped transition.

As we conduct Lagrangian experiments, distance equals time. We define $t_0 = 0\,\mathrm{a}$ at the pRES measurements furthest upstream (Fig. 1) that is also the location of the seismic observations by Hofstede et al. (2021a, b). To evaluate our simulations,

300   we compare the simulated surface topography and ice thickness, as well as $u_z(z)$ with the observed one.
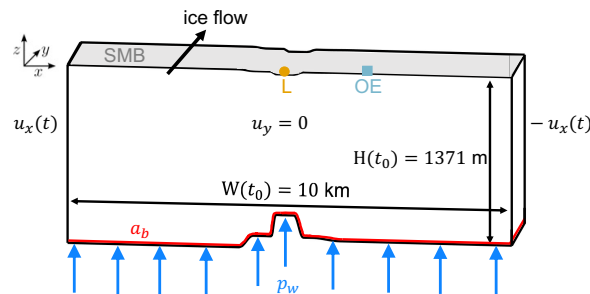
Figure 5. The cross-section of the model geometry at the end of the spin-up (t_0) of the first experiment shows its corresponding width and ice thickness outside east. The boundary conditions of the viscoelastic model are the water pressure p_w acting perpendicular to the ice base, the displacement in the flow direction u_y, which is zero due to plane strain assumptions, and the time-dependent displacement $u_x(t)$ acting in the lateral direction derived by pRES observations. The locations of the pRES station at the lowest point (L) of the channel and outside east (OE) are shown at their position on the surface in addition to the SMB (mass increase) and the melt rate a_b (mass decrease) at the base of the geometry.

We performed a spin-up to avoid model shocks, introduced by the transient behavior of a Maxwell material, that could be falsely interpreted as the response. The main goal ~~is~~ here is to have the geometry after spin-up fit reasonably to the geometry measured at the seismic IV line (see Fig. 1) that we denote as time t_0. The spin-up covers $75\,\mathrm{a}$, which corresponds to the time from the grounding line to that profile under present day flow speeds. To this end, we take a constant melt rate equal to the melt

305   rate at t_0 and adjust the geometry at the grounding line to match the geometry at t_0 of the seismic IV profile reasonably well. After the spin-up, the width $W(t_0)$ of the simulated geometry is $10\,\mathrm{km}$. With this procedure an initial elastic deformation at the beginning of the transient simulation vanished and the viscoelastic geometry evolution of the melt channel can be evaluated for different melt ~~scenarios,~~

Short-term forces like the time-varying climate forcing as well as the lateral extension or compression demand the usage

310   of a viscoelastic instead of a viscous model to simulate the temporal evolution of the basal channel. We conduct a series of simulations with different material parameters and identify the best match of observed and simulated ice thickness above (L) and outside east (OE) of the channel. At these two positions most of the pRES measurements were done and the distribution of the melt rates gives an adequate basis to force the model. Due to the sparsity of observations at the western side, we apply a forcing in the model based only on melt rates at L and OE.

315   In a first experiment, we use an interpolation of the observed melt rates as forcing and compare the results with H_{PDadv} (solid

lines in Fig. 3). The second experiment aims to derive the best match between simulated and observed geometry. For this experiment, we use synthetic melt rates (dashed lines in Fig. 3a).

3.2 Results and discussion of simulations

3.2.1 First experiment: pRES-derived melt rate

320   The spin-up for this experiment ~~is~~ starts with a manually adjusted geometry (including the channel at the base) for $t = -75\,\mathrm{a}$ to fit seismic IV profile for t_0 at the base. We applied a constant melt rate of $1.5\,\mathrm{m\,a}^{-1}$ at L and $0.5\,\mathrm{m\,a}^{-1}$ at OE. This forcing enlarges the melt channel during the spin-up as the ice thickness OE increases due to the prescribed displacement at the lateral boundaries. The general shape of the base matches the seismic profile IV reasonably well (Fig. 1 and Fig. B3). ~~In the experiment,~~ we force the base with a_b (solid line in Fig. 3a).

325   The results of this experiment are displayed in Fig. 6. For both locations, L and OE, the simulated and observed geometry differ significantly. While the simulated ice thickness above the channel only declines by $21\,\mathrm{m}$ or 1.7% in $250\,\mathrm{a}$, the observed one is a factor of 9, or $191\,\mathrm{m}$ thinner. However, the simulated trend outside the channel shows thinning. This thinning sets in after $50\,\mathrm{a}$, whereas we find continuous thinning in the observations. This delayed onset of thinning is also represented in the simulated surface topography. Most notably is the match between simulated H_sim and advected H_PDadv ice thickness under

330 present day climate conditions at L. This match confirms that present day melt rates would not lead to the observed channel evolution over $250\,\mathrm{a}$.

3.2.2 Second experiment: Synthetic melt rate

The spin-up for the second experiment also starts with a geometry that has been manually adjusted for $t = -75\,\mathrm{a}$ to fit seismic IV profile for t_0 at the base. In the second simulation experiment, we force the base with the synthetic melt rate (Fig. 3a).

335 Again, the melt rate has been kept constant over the spin-up with $a_b^\mathrm{syn}(t_0)$. By disregarding the additional melt of the spin-up, the synthetic melt rate leads to a cumulative melt after $250\,\mathrm{a}$ of $290\,\mathrm{m}$ (Fig. B2a). With that $184\,\mathrm{m}$ more ice is melted at L than in the first experiment.

    The modeled geometry of this experiment is presented in Fig. 7. The simulated ice thickness at L is in very good agreement with H_pRES. There is some mismatch at OE, but the simulated trend of thinning is synchronous to the observation. After

340 $250\,\mathrm{a}$ the deviation from the observed ice thickness at OE reaches $53\,\mathrm{m}$. The simulated evolution of the base for the second experiment shows a persistent basal channel (Fig. B4). The mismatch of the surface elevation at L and OE is reversing over time: while the simulated surface topography at OE is first too low, it is too high in the second half of the transient simulation (Fig. 7). However, the trend of the observed h_TDX and simulated h_sim elevation behave similarly. Above the channel, the surface elevation is first overestimated by $4\,\mathrm{m}$ at the end of the spin-up. After $57\,\mathrm{a}$, it turns from an over- to underestimation

345 that results in an $8\,\mathrm{m}$ lower h_sim than the observed h_TDX after $250\,\mathrm{a}$. To assess if the ice is in buoyancy equilibrium, we compute the freeboard at the position L for an ice density of $910\,\mathrm{kg\,m}^{-3}$. The surface elevation is $133\,\mathrm{m}$ at t_0 and decreases to $112\,\mathrm{m}$ after $250\,\mathrm{a}$. Although h_TDX is larger than this, the ice is approaching flotation in downstream direction. One could
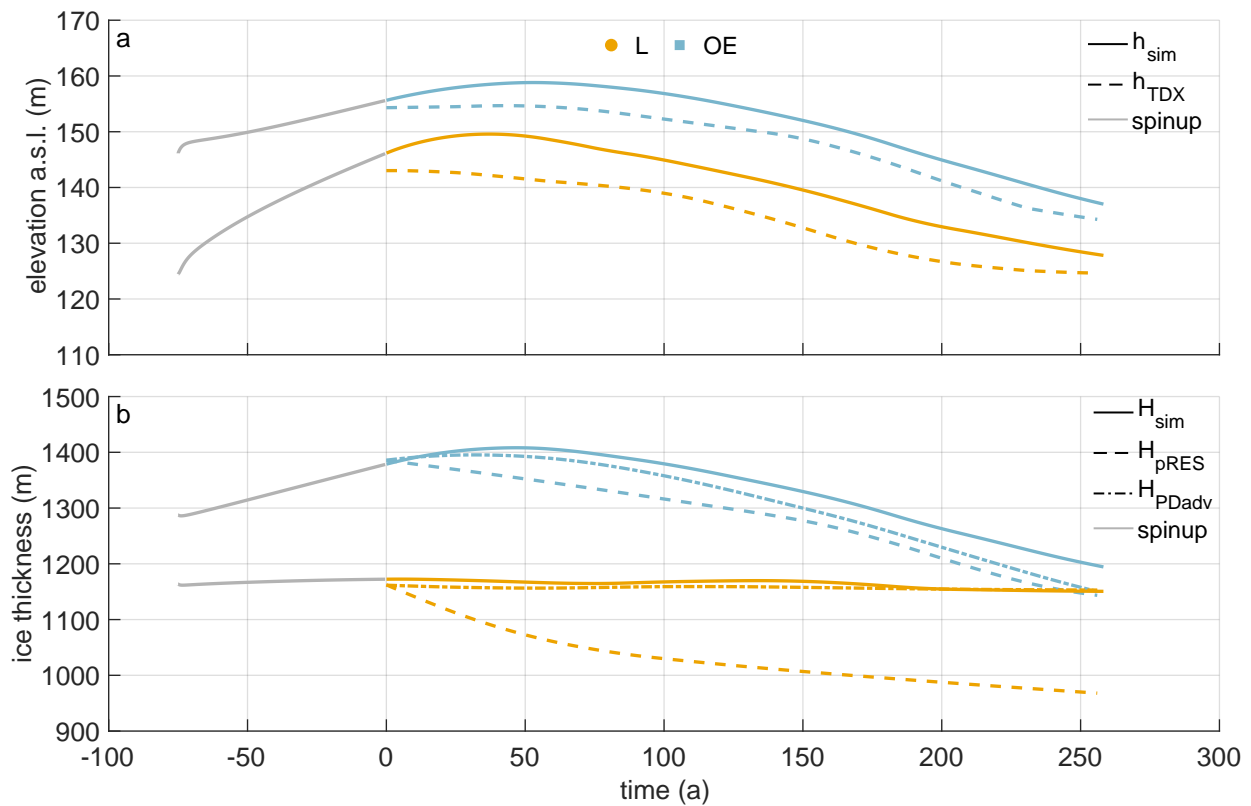
Figure 6. First experiment: Simulated surface elevation (a) and ice thickness (b) using the pRES-derived melt rate. Colors denote quantities above the channel (yellow) and outside the channel (blue). (a) Simulated surface elevation h_{sim} (solid lines) and observed h_{TDX} (dashed lines). (b) Simulated ice thickness H_{sim} (solid lines), under present day climate conditions advected H_{PDadv} (dashed-dotted lines) and observed H_{pRES} (dashed lines). Gray lines represent the spin-up.

take another approach and estimate the mean density under the assumption of buoyancy equilibrium: at t_0 this corresponds to $901 \, \text{kg} \, \text{m}^{-3}$ and after $250 \, \text{a}$ to $896 \, \text{kg} \, \text{m}^{-3}$. As more ice is melted from below and with higher snow accumulation at L, the

350   density decreases, which is to be expected.

     After $250 \, \text{a}$, the simulated freeboard at OE is $1 \, \text{m}$ higher than the surface elevation of $138 \, \text{m}$ inferred by buoyancy equilibrium using an ice density of $910 \, \text{kg} \, \text{m}^{-3}$. Similar considerations regarding OE lead to a $3 \, \text{m}$ higher h_{TDX} than $132 \, \text{m}$ out of buoyancy equilibrium. Overall, we see convergence to equilibrium state at OE and the simulated surface elevation at L. At the end of the simulation, only h_{TDX} above the channel does not reach buoyancy equilibrium, which leads to the justifiable assumption that

355   the mean ice density at L is lower than OE.

     At the position of the furthest upstream pRES observations we can see from the seismic IV profile that the influence of the grounding line has not completely vanished. The assumption of buoyant equilibrium is therefore likely to be flawed. At the
end of the simulation, the geometry should be close to buoyancy equilibrium despite melting and a 50% higher SMB at L than
OE. Hence, simulations carried out using a higher SMB within the channel would result in better agreement with the observed
360 values of h_{TDX}.
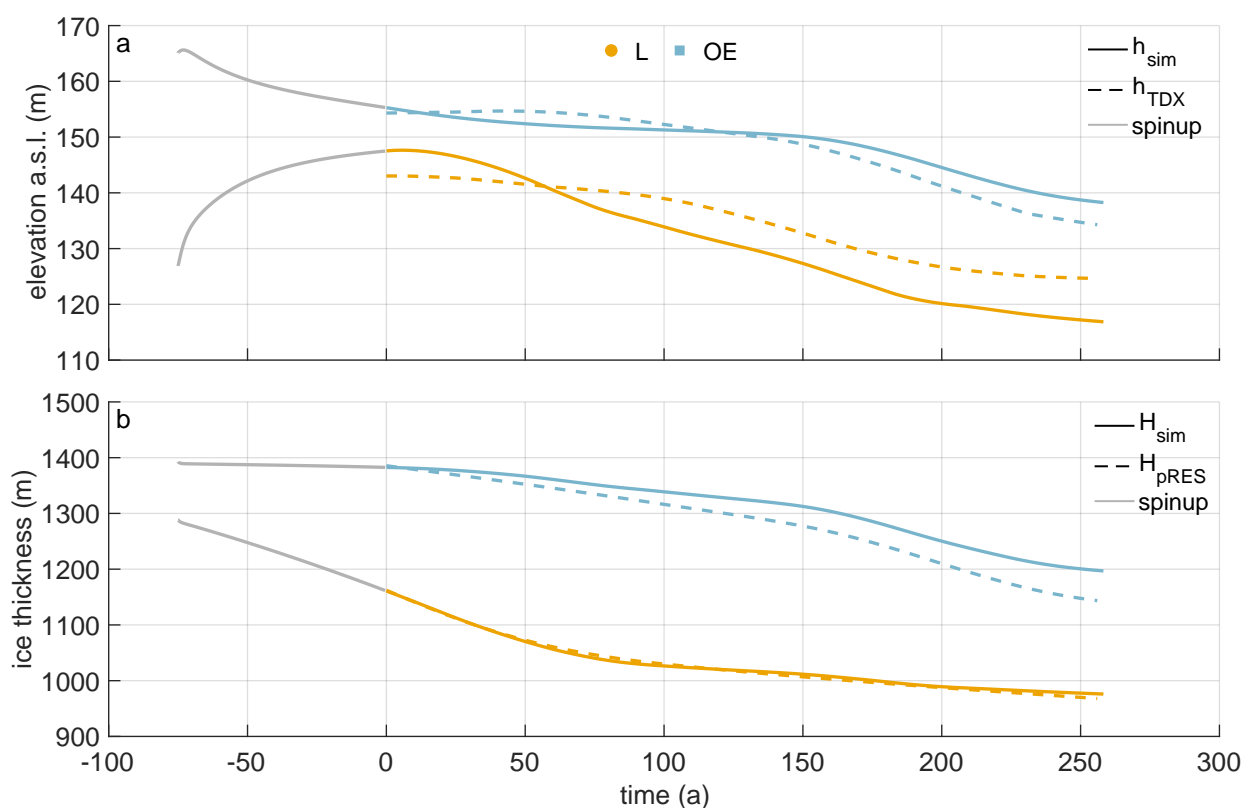
Figure 7. Second experiment: simulated surface elevation (a) and ice thickness (b) using the synthetic melt rate. Colors denote quantities above the channel (yellow) and outside the channel (blue). (a) Simulated surface elevation h_{sim} (solid lines) and observed h_{TDX} (dashed lines). (b) Simulated ice thickness H_{sim} (solid lines) and observed H_{pRES} (dashed lines). Gray lines represent the spin-up.

Next, we exploit the variation of the vertical displacement over depth. The results are presented in Fig. 8. For this purpose, we calculated the cumulative vertical displacement in one year over depth. For comparability, the vertical displacements due to accumulation and snow compaction were removed from the observed distributions.

365 Most notably, we move from a vertically extensive regime into a compressive by increasing distance to the grounding line. Given the complexity of the problem, the simulations show a reasonable agreement with the observations. The best match is reached at OE, which is not that surprising. The generally good agreement of the simulated displacements outside the channel comes from tuning u_x at the lateral boundary to match u_z from the pRES measurements at OE. Both simulated and observed
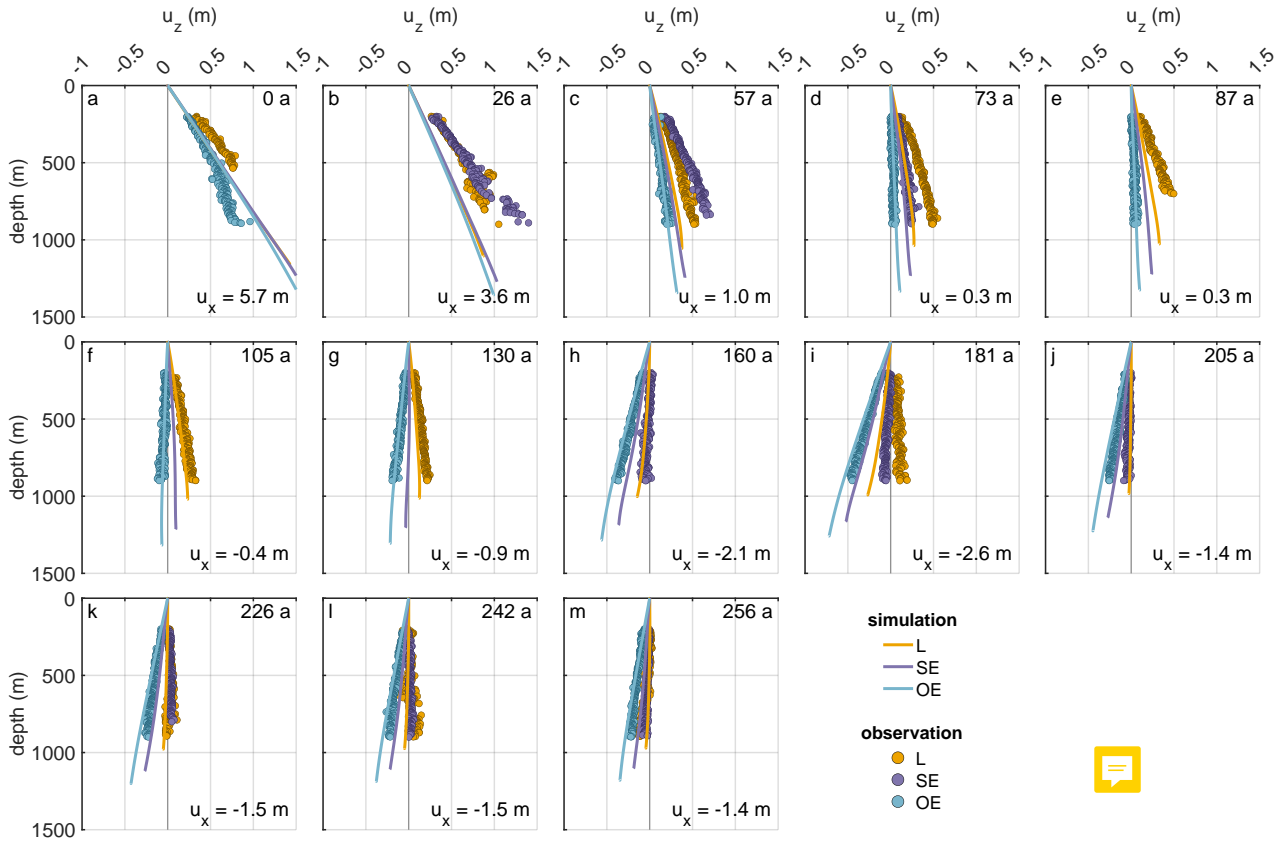
Figure 8. Second experiment: comparison of displacements (u_z) derived from observations (dots) and the simulations (lines). The different panels show the displacement for $\Delta t = 1\,\text{a}$ allocated to the simulation time (number in the upper right corner). The numbers in the lower right corners give horizontal displacement u_x derived from ε_{zz} of the pRES measurements outside the channel (OE) with positive values representing compression and negative values extension.

vertical displacement distributions show that the strain decreases from L to OE. The only exception here is $t = 57\,\text{a}$, where the

370   vertical strain at SE is larger than the one at L. While at $0\,\text{a}$ and $26\,\text{a}$ the deviation of the simulated displacements between L and OE is small, it increases afterwards. From $105\,\text{a}$, the simulated vertical displacements agree very well with those of the pRES-measurements, where a displacement distribution was derivable at L and OE. The same comparison for the first experiment (Fig. B5) shows similar results, with significantly less pronounced differences between L and OE. Hence, the mismatch to the observed vertical displacements for this experiment using the measured melt rates is higher than for the second experiment

375   with the synthetic melt rates. The simulated strain evolution of the cross-section confirms that the viscoelastic model needs to account for finite deformation as the strain exceeds 10% (Fig. B6).

As the last point of this second experiment, we consider the influence of the viscosity on the evolution of the melt channel (Fig. B7). To reach the ice thickness of seismic IV, the simulation applying the smallest viscosity needs a higher initial channel and hence, less ice thickness at L at the beginning of the spin-up (Appendix Sec. B2). The channel thickness of the pRES-

380 measurement is modeled best using a viscosity of $5 \times 10^{15}\,\mathrm{Pa\,s}$. A two times higher viscosity leads to an ice thickness in the channel that is $42\,\mathrm{m}$ smaller after $250\,\mathrm{a}$, while a five times lower viscosity results in $116\,\mathrm{m}$ thicker ice above the channel due to more viscous flow into the channel. The simulated ice thickness OE is similar for all three different viscosities.

4 Discussion

Melt rates inside the channel are in general rather moderate $< 2\,\mathrm{m\,a^{-1}}$. For comparison values retrieved at a channel $1.7\,\mathrm{km}$

385 from the grounding line of the Ross Ice Shelf at Mercer Whillans ice streams inflow were $22.2\,\mathrm{m\,a^{-1}}$ (Marsh et al., 2016). At the Ross Ice Shelf, the values dropped to below $4\,\mathrm{m\,a^{-1}}$ over a distance of $10\,\mathrm{km}$ and reached $2.5\,\mathrm{m\,a^{-1}}$ after $40\,\mathrm{km}$. We also find a factor of five lower values in the center of the channel over a distance of $11\,\mathrm{km}$, however, this takes place between 14 and $25\,\mathrm{km}$ downstream the grounding line. However, at about the same distance, we find a peak in basal melt rate of $2.3\,\mathrm{m\,a^{-1}}$ (Figs. 1 and 2) at OE. Interestingly enough, this location corresponds to a steep basal topography in the seismic profiles I and

390 V, indicating that we might have not been entirely outside the channel at this spot, but potentially at a steep flank. At the Ross Ice Shelf, the ratio between inside the channel and $1\,\mathrm{km}$ outside is about 27, whereas we find only a factor of 3, with a distance between L and OE being $1.8\,\mathrm{km}$. Zeising et al. (2021) presented pRES-derived basal melt rates downstream of our study area. Roughly $40\,\mathrm{km}$ downstream the northernmost cross-section ($\sim 200\,\mathrm{a}$ of ice flow), these measurements show that the channel still exists, but with a small height of $\sim 16\,\mathrm{m}$. Inside the channel, Zeising et al. (2021) determined a melt rate of $0.25\,\mathrm{m\,a^{-1}}$

395 and outside $0.41\,\mathrm{m\,a^{-1}}$. The larger melt rates outside the channel compared to inside is in agreement with the finding of our study. In general, the channel height declines, so the channel fades out. The channel diminishes by melt rates inside the channel falling below those outside the channel. The trend in vertical strain has only a minor contribution to this evolution. We thus do not find any evidence that such channels are a cause for instabilities of ice shelves as suggested by Dow et al. (2018).

One of the main findings of our study is that the present geometry can only be formed with considerable higher melt rates in

400 the past (see Fig. 3). This finding is based on the assumption that the strain-rates were in the past similar to present day. This is justified, as significant changes in strain would require a change in the system that would cause other characteristics to change, like the main flow direction, for which we do not find any indication.

The pRES melt rate observations covered only one year. As the ocean conditions within the sub-ice shelf cavity are known to respond to the ocean forcing from the ice front (e.g. Nicholls, 1997), they would expect to be subject to significant interannual

405 variability. Underlying any interannual variability, a long-term reduction in basal melt rates would be the expected response to a reduction in production of dense shelf waters north of the ice front, resulting from a reduction in sea ice formation (Nicholls, 1997), resulting in turn from a reduction in the southerly winds that blow freshly produced sea ice to the north.

A decrease in northward motion of sea ice has been observed in the satellite record (e.g. Holland and Kwok, 2012), and modeling experiments by Naughten et al. (2021) find decreasing basal melt rates. This reduction is therefore consistent with

410 higher basal melt rates in the past. However, our model results suggest that the mismatch between the past melt rates needed to explain the observed channel geometry and those that were observed applies only to the channel, and not to the ambient ice. This could be explained by historically higher levels of subglacial outflow at the grounding line, or anomalously low levels during the observation period. Subglacial outflow contributes to the buoyant flow up the basal slope and therefore the shear-induced turbulence that raises warm water from deeper in the water column towards the ice base. Smith et al. (2009) found

415 an active subglacial lake at the transition between Academy Glacier and SFG, and also Humbert et al. (2018) suggest in the upstream area of SFG a subglacial lake.

Hofstede et al. (2021a) showed that the subglacial channel appears $7\,\mathrm{km}$ upstream of the grounding line increasing its height to $280\,\mathrm{m}$ at the grounding line. The location of the channel corresponds with increased subglacial flux found by Humbert et al. (2018) using a simple routing scheme. The channel formed on the grounded part is most likely the source of a grounding line

420 fan and thus carrying sediments, formed at the seabed under the basal channel Hofstede et al. (2021a). Once this topographic feature reaches the ocean, it will focus on the relatively buoyant flow and enhance shear-driven vertical mixing, bringing heat and salt to the ice base leading to higher basal melt rates.

However, with increasing distance along the channel, the basal gradient, and therefore the speed of the buoyant flow, reduces, as does the entrainment of warm water from beneath. Coupled with the increasing pressure freezing point at the ice base this

425 leads to a gradual reduction of the melt rate in the channel. From Fig. 2a, the melt rate in the channel reduces below that of the ambient ice base by about $30\,\mathrm{km}$ distance from the grounding line, suggesting that the effect of basal melting thereafter is to suppress the channel. The cause of the strong melt anomalies identified in the ApRES measurements remains unclear as no direct ocean observation exists near SFG. However, the time scale of the events is consistent with the passage of warm cored eddies. Such features have been observed in the ocean cavity beneath the neighboring Ronne Ice Shelf (Nicholls, 2018).

430 The channel height is found to increase until 30–$35\,\mathrm{km}$ downstream of the grounding line. Further downstream, the channel begins to close. Our modeling results show that less viscous ice ($1 \times 10^{15}\,\mathrm{Pa\,s}$) would tend to shut the channel faster than the rate we observe. For the best match between observed and modeled geometry, we need viscosities around $5 \times 10^{15}\,\mathrm{Pa\,s}$ of stiff ice to prevent the closure by deformation. This claim is also confirmed by the inversion of the viscosity to model observed surface velocities in the melt channel region (Appendix Sec. B1). With a viscosity of $5 \times 10^{15}\,\mathrm{Pa\,s}$, we can simulate with a

435 viscoelastic model the channel evolution in both experiments matching the observations: (i) pRES-derived melt rates result in an ice thickness fitting the present day advected ice thickness H_{PDadv}, (ii) synthetic melt rates lead to the observed ice thickness H_{pRES}.

The difference in geometry change, due to different values of the viscosity, manifests stronger inside the channel than outside. This was to be expected because of the load situation resulting from the prescribed geometry (Fig. B7). The simulated geometry

440 change is mainly due to the elastic response to thinning by basal melt and ice accumulation. Any purely viscous simulation would overrate the deformation. Higher melt rates were needed to compensate for this. Wearing et al. (2021) presents a full Stokes simulation of a comparable melt channel and indeed needs high melt rates to keep the channel open. It is important to keep this result in mind for (future) inverse modeling of melt rates in melt channels.

We find a difference ($-4\,\mathrm{m}$ to $8\,\mathrm{m}$) between simulated and observed surface elevation at L. The elevation difference is most

445 likely caused by the constant density that we used for the simulations, as the ice thickness matches well. For the thinner ice above the channel, this could be achieved by an ice density decreasing from outside to inside and from upstream to downstream the channel. However, one has to keep in mind, that the accuracy of the surface elevation product is $5\,\mathrm{m}$.

In general, we benefited highly from having measurements of vertical strain available. This opens new possibilities to identify weaknesses in the modeling and gave us useful insight into the spatial variation of the vertical strain across such a topographic

450 feature. Although the pRES surveys only about half the ice thickness, the slope of $u_z(z)$ in the upper half is distinct for the positions L, SE and OE and greatly varies with distance from the grounding line, also influenced by the embayment of the ice shelf. Simulated u_z at L start to match only after about $100\,\mathrm{a}$ well with observations, which could result from the first few cross-sections still being influenced by the hinge zone. Tidal bending was not taken into account here, due to the 2D setting. This could in future be investigated, if repeated pRES measurements would be conducted up to the grounding line covering the

455 entire hinge zone, in which it would also be extremely advantageous to obtain basal melt rates.

Our study demonstrates that viscoelastic simulations can be a useful but complex tool to analyze melt channel evolution. In an inverse approach, viscoelastic models could also give more insights into basal melt rates of channel systems of ice shelves in general, given that satellite-borne surface elevation is available in high resolution. However, the fact that large deformations require non-linear strain theory will make this a challenging endeavor. As changes in basal melt rates will inevitably lead to

460 surface elevation changes of channel systems, systematic monitoring of the surface topography from space can serve as an early warning system and trigger further in-situ observation similar to this study.

5 Conclusions

We find basal melt rates in a melt channel and its surroundings on Filchner Ice Shelf to be up to $2.3\,\mathrm{m\,a^{-1}}$. Basal melt rates inside the channel drop with distance down-flow, even turning into freezing $55\,\mathrm{km}$ downstream of the grounding line. Close to

465 the grounding line, melt rates are larger inside the channel than outside, while further downstream this relationship reverses. Over distance along flow, the channel dimension decreases from a maximum height of $330\,\mathrm{m}$ to below $100\,\mathrm{m}$. The channel diminishes because the reduced melt rate is unable to maintain the channel geometry against viscoelastic deformation. Analysis of the present day ice thickness advection revealed large differences compared to the observed ice thickness above the channel, which indicates that melt rates have been about twice as large in the last $250\,\mathrm{a}$. The viscoelastic simulation confirms this

470 statement and indicates that basal melt channels need high basal melt rates and relatively cold ice to persist. The deformation of the basal melt channel is mainly driven by the elastic response to the basal melt rate. The observed and simulated evolution of this melt channel demonstrates that melt channels of this kind are not a destabilizing element of ice shelves. The ApRES time series showed brief melt anomalies distributed over the entire measurement period and slightly increased melt rates in summer.

475 *Code availability.* The mph file of the finite element software COMSOL Multiphysics (Version 5.6) of the viscoelastic finite deformation
simulation used for this study is available via AWI's gitlab (https://gitlab.awi.de/jchristm/viscoelastic-finite-defos-meltchannel).

Data availability. Raw data and derived products of the single-repeated pRES measurements, raw data of the ApRES time series (https://doi.
pangaea.de/10.1594/PANGAEA.932413), surface accumulation data at pRES locations, processed GPS measurements (https://doi.pangaea.
de/10.1594/PANGAEA.932441 are submitted to the World Data Center PANGAEA. The seismic data (https://doi.org/10.1594/PANGAEA.
480 932278) are available at the World Data Center PANGAEA (Hofstede et al., 2021b). BedMachine Antarctica product can be accessed
at http://nsidc.org/data/nsidc-0756200 (Morlighem, 2020) (last access: 12 April 2021) MEaSUREs velocity product can be accessed at
https://nsidc.org/data/nsidc-0754/versions/1 (Mouginot et al., 2019a) (last access: 13 April 2021).

Appendix A: Observations

A1   Additional table

Table A1. Description of symbols

Symbol	Description
u_x	horizontal displacement in across flow
u_y	horizontal displacement in along flow
u_z	vertical displacement
ε_{xx}	horizontal strain in across flow
ε_{yy}	horizontal strain in along flow
ε_{zz}	vertical strain
$\overline{h_b}$	averaged depth of the ice base
h_{pc}	depth of the pore closure relative to surface
h_{nl}	noise-level depth limit relative to surface
h_{sim}	simulated surface elevation
h_{TDX}	TanDEM-X surface elevation
H	ice thickness
H_{pRES}	pRES derived ice thickness
H_{sim}	simulated ice thickness
H_{PDadv}	advection of the ice thickness under present day climate conditions
t	time
t_0	$t = 0\,\mathrm{a}$, defined at the most upstream pRES measurement location
t_1	1st measurement of ApRES time series
t_i	i-th measurement of ApRES time series
Δt	time period between repeated measurements
ΔH	change in ice thickness
ΔH_i	change in ice thickness below the depth of the pore close
ΔH_s	change in ice thickness at the surface and in the firn
ΔH_f	change in ice thickness due to firn compaction
ΔH_ε	change in ice thickness due strain
ΔH_b	change in ice thickness due to basal melt
a_b	basal melt rate
a_b^{syn}	synthetic basal melt rate
W	width of the cross-section in simulations

485 **A2 Additional figures**
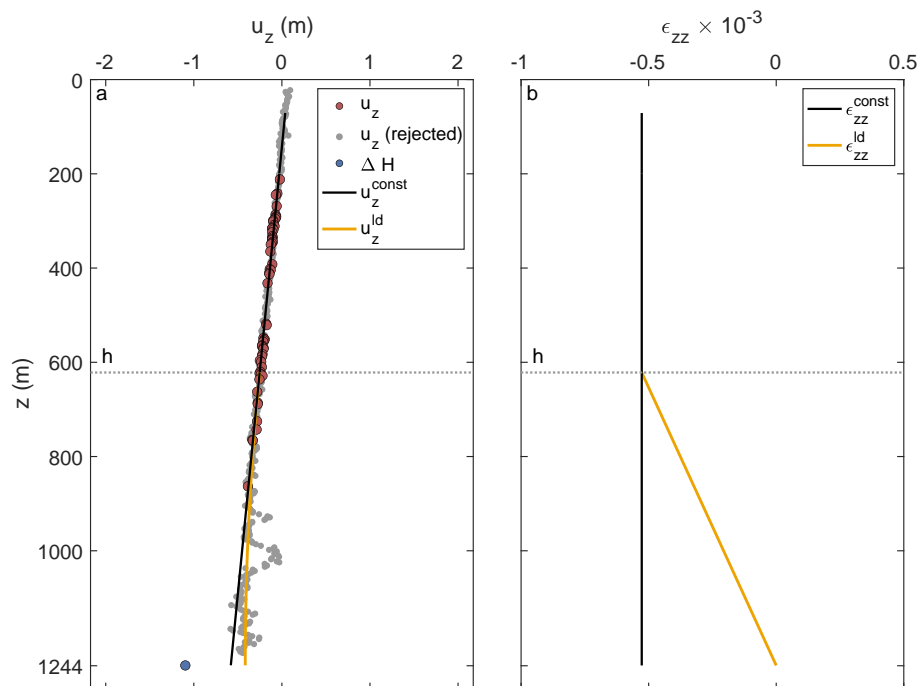
Figure A1. Strain analysis of an pRES measurement. (a) Derived vertical displacements u_z for $\Delta t = 1\,\mathrm{a}$ of the ice base (ΔH; blue dot) and internal layers (red and gray dots). Displacements used for the linear regression u_z^{const} (black line) are colored in red and rejected displacements are shown in gray. The second model u_z^{ld} with a linear decreases (ld) from depth h (dotted line) to zero at the ice base is shown in orange. (b) Vertical strain for $\Delta t = 1\,\mathrm{a}$ of both models whose displacement is shown in (a).
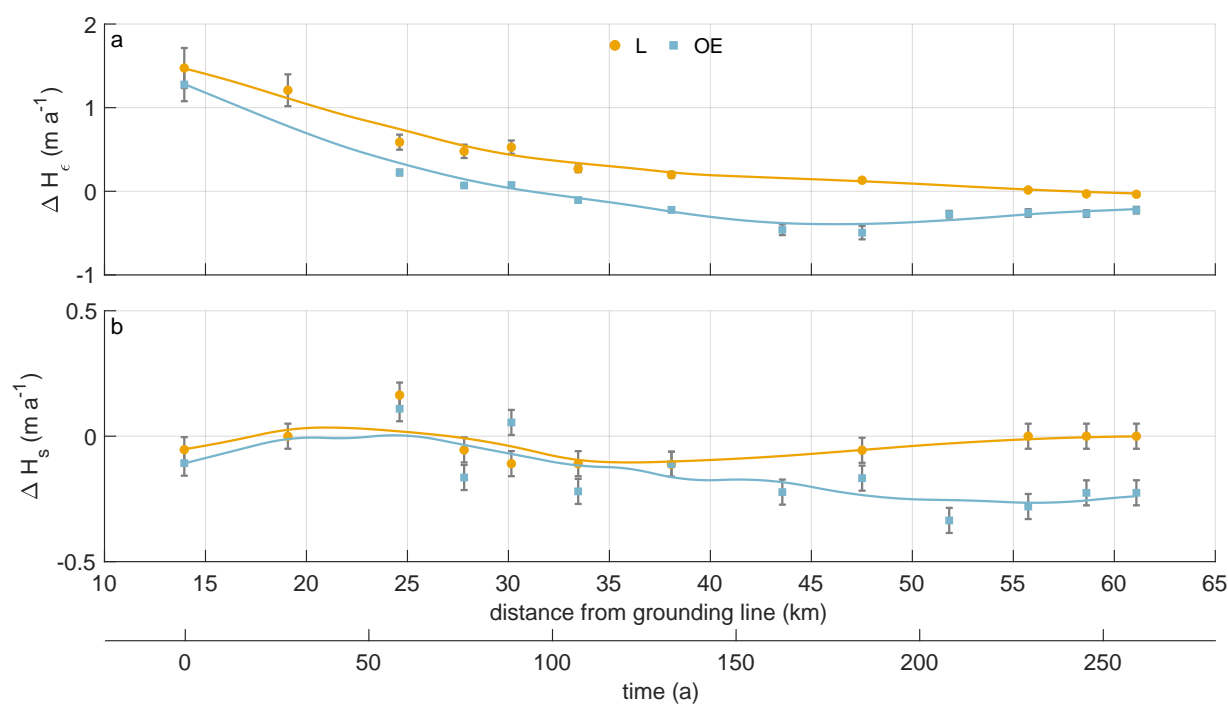
Figure A2. Distribution of pRES-derived (a) change in ice thickness due to strain and (b) ice thickness change due to surface process (firn compaction and accumulation) above the channel (yellow dots) and outside east of the channel (blue squares). The solid lines represent a smoothed fit. Error bars mark the uncertainties of the pRES-derived values.
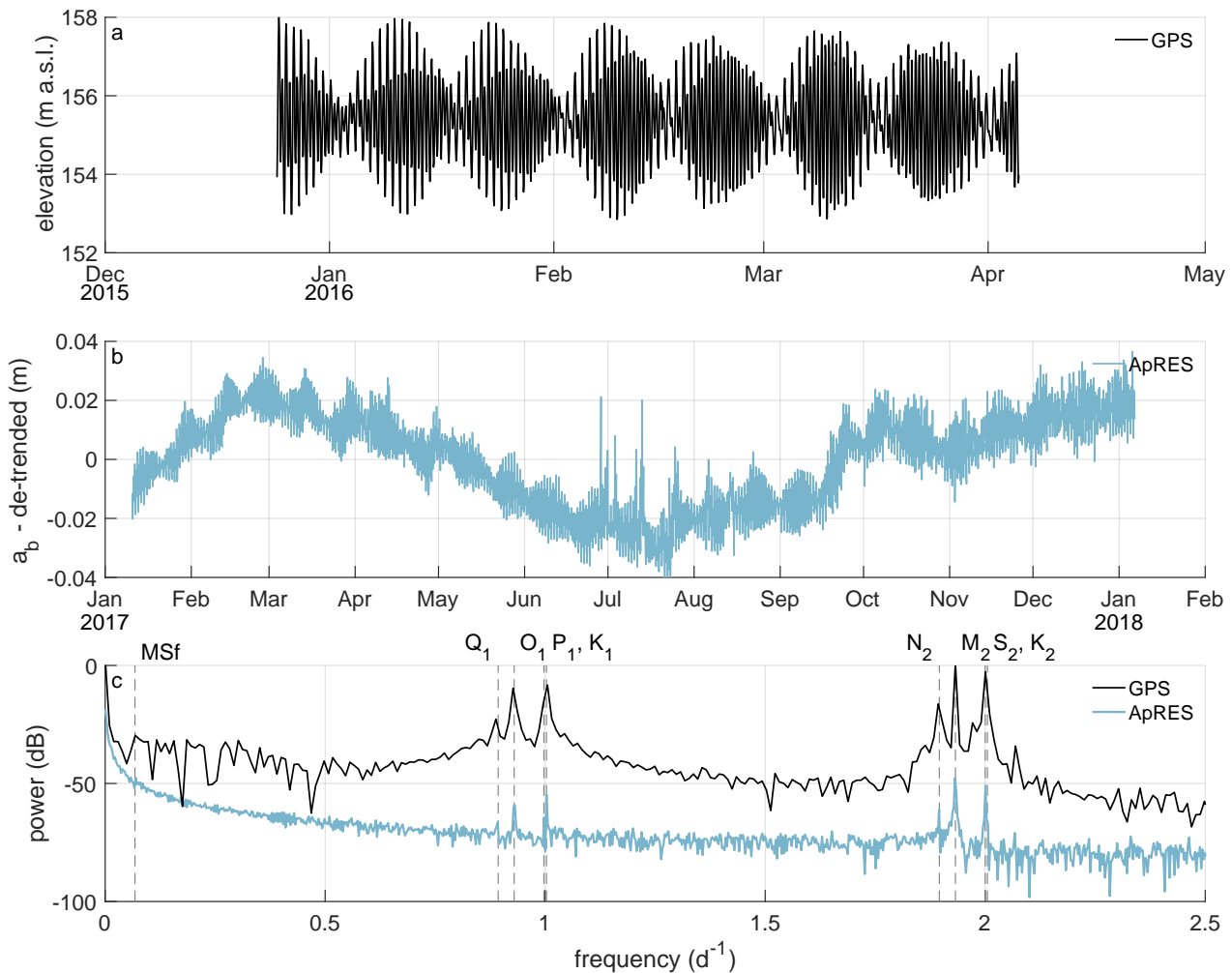
Figure A3. (a) Surface elevation recorded by the GPS station from end of December 2015 to early April 2016. (b) Linear de-trended basal melt rate (a_b) from ApRES observations between January 2017 and January 2018. (c) Frequency spectrum from data shown in (a) and (b). Vertical gray dashed lines mark the constituents with half day periods ($N_2 = 12.66$ h, $M_2 = 12.42$ h, $S_2 = 12.00$ h, $K_2 = 11.97$ h), daily periods ($Q_1 = 26.87$ h, $O_1 = 25.82$ h, $P_1 = 24.07$ h, $K_1 = 23.93$ h), and Fortnightly period (MSf $= 14.76$ d). Notice, due to a shorter measuring period of the GPS, the resolution in frequency space is lower than of the ApRES.

Appendix B: Modeling

B1 Viscosity from inverse modeling

For estimating the viscosity distribution in the Filchner-Ronne Ice Shelf, we conduct a control-method inversion for the rheology parameter in the floating part. We use the Ice Sheet and Sea Level System Model (Larour et al., 2012) applied to the
490 Filchner-Ronne Ice Shelf using the Blatter-Pattyn higher-order approximation (Blatter, 1995; Pattyn, 2003). The calculation is done on an unstructured finite element grid with a refined resolution of $2\,\mathrm{km}$ at the grounding line, in the shear margins as well as at other regions of faster ice flow. In the melt channel domain we further refine the resolution of the grid to $0.5\,\mathrm{km}$.
To generate the geometry of the ice shelf the BedMachine Antarctica v2 data set is used (Morlighem et al., 2020; Morlighem, 2020). For the ice rigidity in the grounded region, as well as an initial guess of ice rigidity in the floating shelf, we assume the
495 results of a long-term thermal spin-up also used in Eisen et al. (2020) based on the geothermal flux from Martos et al. (2017). We constrain ice surface velocities to fit the MEaSUREs data set (Mouginot et al., 2019b, a).
Our optimization approach iteratively infers two parameters – the basal friction parameter in the grounded area and the ice rheology parameter in the floating area. For this purpose two cost functions are built. Each cost function consists of two data misfits, linear and logarithmic, as well as a Tikhonov regularization term:

500
$$J(\boldsymbol{v}, k) = \gamma_1 \int\limits_S \frac{(v_x - v_x^{\mathrm{obs}})^2 + (v_y - v_y^{\mathrm{obs}})^2}{2} \,\mathrm{d}S + \gamma_2 \int\limits_S \left(\log \left(\frac{||\boldsymbol{v}|| + \varepsilon}{||\boldsymbol{v}^{\mathrm{obs}}|| + \varepsilon} \right) \right)^2 \mathrm{d}S + \gamma_t J_{\mathrm{reg}} \tag{B1}$$

The first term will be most sensitive to velocity observations in fast-flowing areas, the second term will be most sensitive to velocity observations in slow-floawing areas, while the third term penalizes oscillations in the optimization parameter. We performed an L-curve analysis to find suitable weights $\gamma_1, \gamma_2, \gamma_t$ for both cost functions. With this trade-off curve, we can make sure that we find a regularization term that fits the data well without overfitting noise. For the basal friction inversion,
505 we found best weights $\gamma_1 = 1$, $\gamma_2 = 5 \times 10^{-6}$ and $\gamma_t = 1 \times 10^{-8}$, while for the ice rigidity inversion the optimal weights were $\gamma_1 = 1, \gamma_2 = 0.8$ and $\gamma_t = 4 \times 10^{-17}$.
We linearize and solve the optimization problem using the M1QN3 algorithm with an incomplete adjoint (Larour et al., 2012). For this inversion setting we apply a gradient relative convergence criterion $\epsilon_{\mathrm{gttol}} = 10^{-6}$ and two points which are less then $\mathrm{dxmin} = 10^{-4}$ from each other are considered identical. Besides we used a maximum number of iterations and function eval-
510 uations of 1000. We show our best-fit results for ice viscosity in the region around the melt channel in Fig. B1. The range of the viscosity is between 5.0563×10^{13} and $2.6656 \times 10^{15}\,\mathrm{Pa\,s}$.
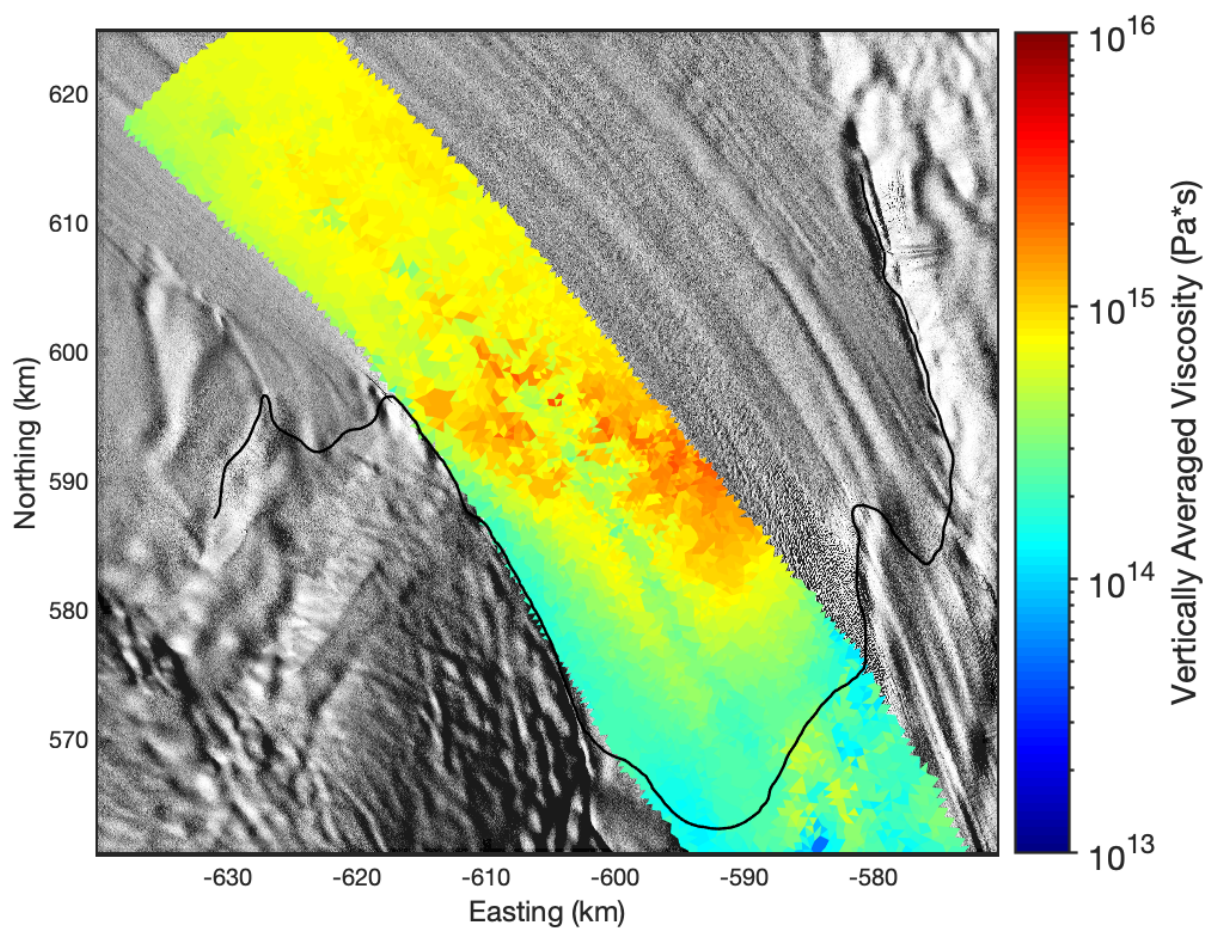
Figure B1. Ice viscosity in the melt channel area obtained from inverse modeling. The map extent is the same as in Fig. 1. The background image is a hillshade of the Reference Elevation Model of Antarctica (Howat et al., 2018, 2019).

B2 Sensitivity of experiment 2 on viscosity

To capture the influence of the viscosity, different constant values (one smaller and one higher as in the second experiment) are investigated in a further experiment. The spin-up for each viscosity starts at $t = -75\,\mathrm{a}$ with an arbitrary basal geometry that should fit seismic IV profile at the end of the spin-up (t_0). The melt rate $a_b^{\mathrm{syn}}(t_0)$ is again assumed to be constant over the spin-up for all different viscosity values. We force the base with the synthetic melt rate (Fig. 3a), the same melt rate we already used in the second experiment. The initial base for the middle and high viscosity is nearly the same as $5 \times 10^{15}\,\mathrm{Pa\,s}$ is for ice a rather high value requiring cold ice (Fig. B7). For the smallest viscosity, a deeper channel at the beginning of the spin-up is needed.

B3 Additional figures

520
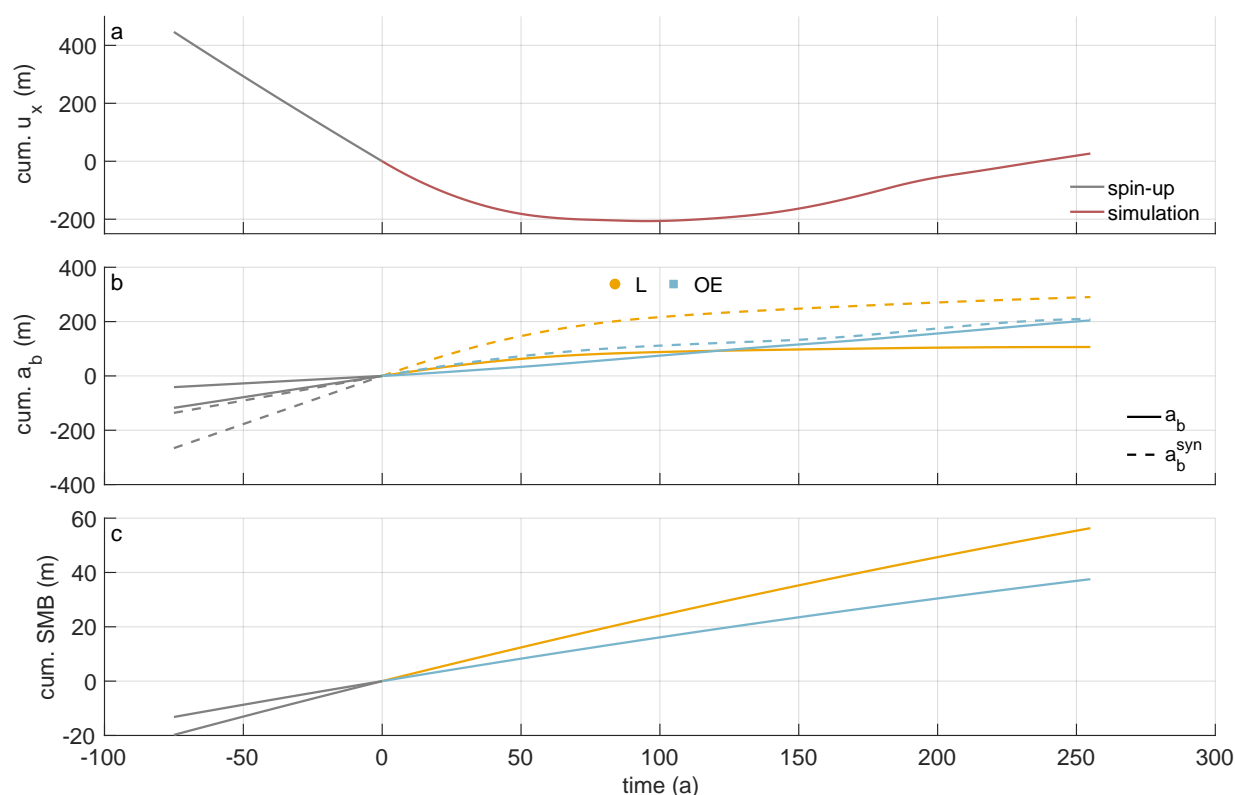
Figure B2. Model input derived from pRES measurements and RACMO van Wessem et al. (2014). (a) Cumulative horizontal displacement calculated from pRES-derived vertical strain rates outside of the channel. (b) Cumulative basal melt rates above (yellow) and outside the channel (blue). Solid lines are derived from the pRES measurements and dashed lines are synthetic melt rates that are necessary to reproduce the measured ice thickness distribution. (c) Cumulative surface mass balance (SMB) derived from multi-year mean RACMO2.3 data van Wessem et al. (2014) for a density of $910\,\mathrm{kg\,m^{-3}}$ outside the channel (blue) and above the channel (yellow), 50% larger. Gray lines represent values used in the spin-up and colored lines values used in the simulation of the evolution of the channel.
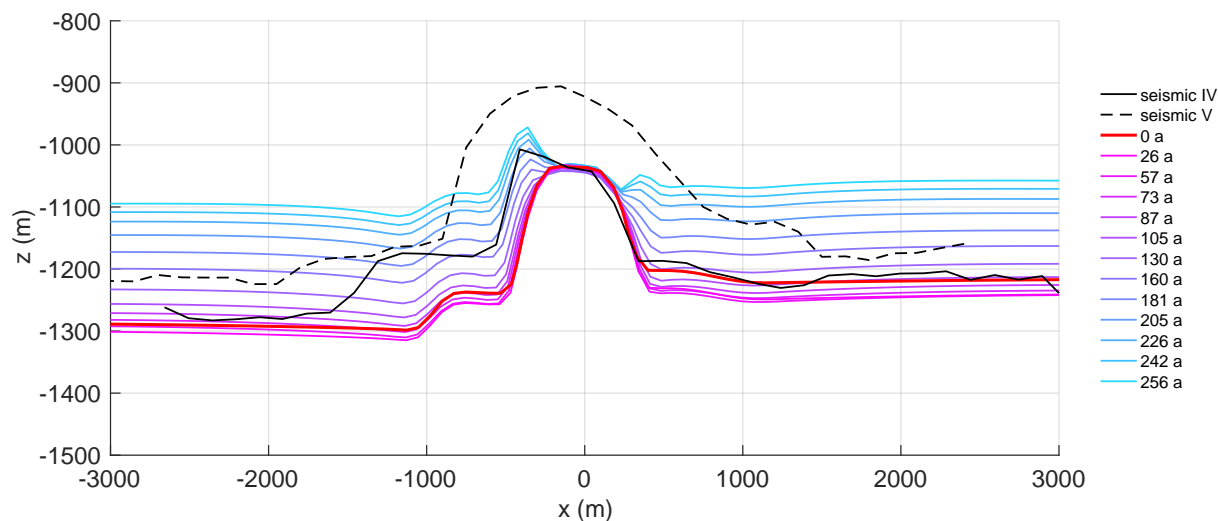
Figure B3. Evolution of the base for the first experiment applying pRES-derived melt rates in the viscoelastic simulation. The black curve shows seismic profile IV Hofstede et al. (2021b) and the red line the simulated base after the spin-up. For each position of pRES observations, the simulated base is shown using a color distribution ranging from red (furthest upstream) to blue (furthest downstream). The dashed black line is the base of seismic profile V Hofstede et al. (2021b) near the pRES observation fitting to $130\,\mathrm{a}$
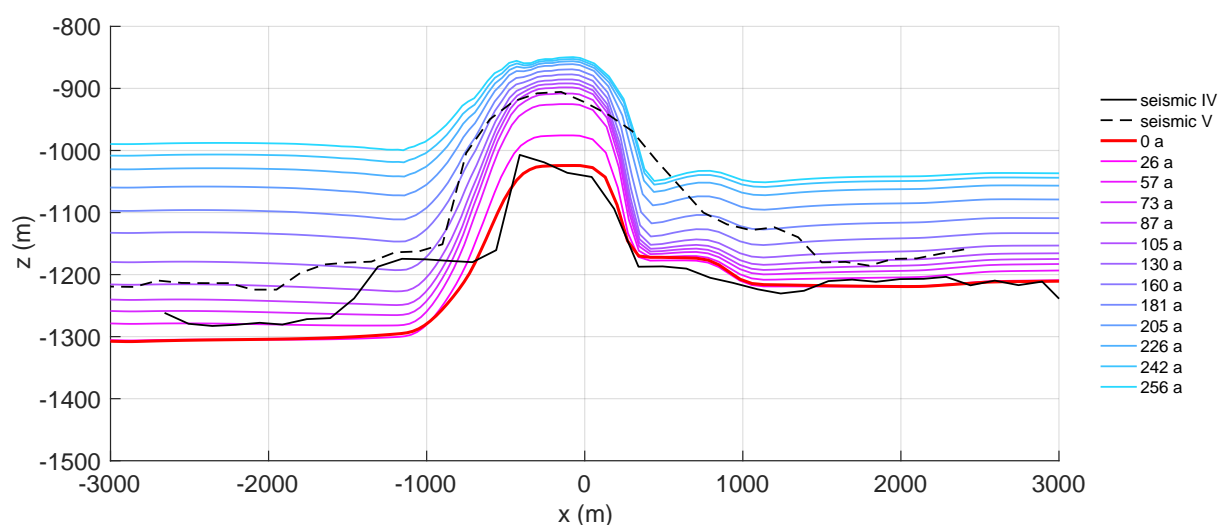
Figure B4. Evolution of the base for the second experiment applying synthetic melt rates in the viscoelastic simulation.The black curve shows seismic profile IV Hofstede et al. (2021b) and the red line is the simulated base after the spin-up. For each position of pRES observations, the simulated base is shown using a color distribution ranging from red (furthest upstream) to blue (furthest downstream). The dashed black line is the base of seismic profile V Hofstede et al. (2021b) near the pRES observation fitting to 130 a. The opening of the basal channel cannot be rebuilt with the model as the melt rate inside the channel is only applied to constant channel width. The basal channel stays open during the simulation time of 256 a.
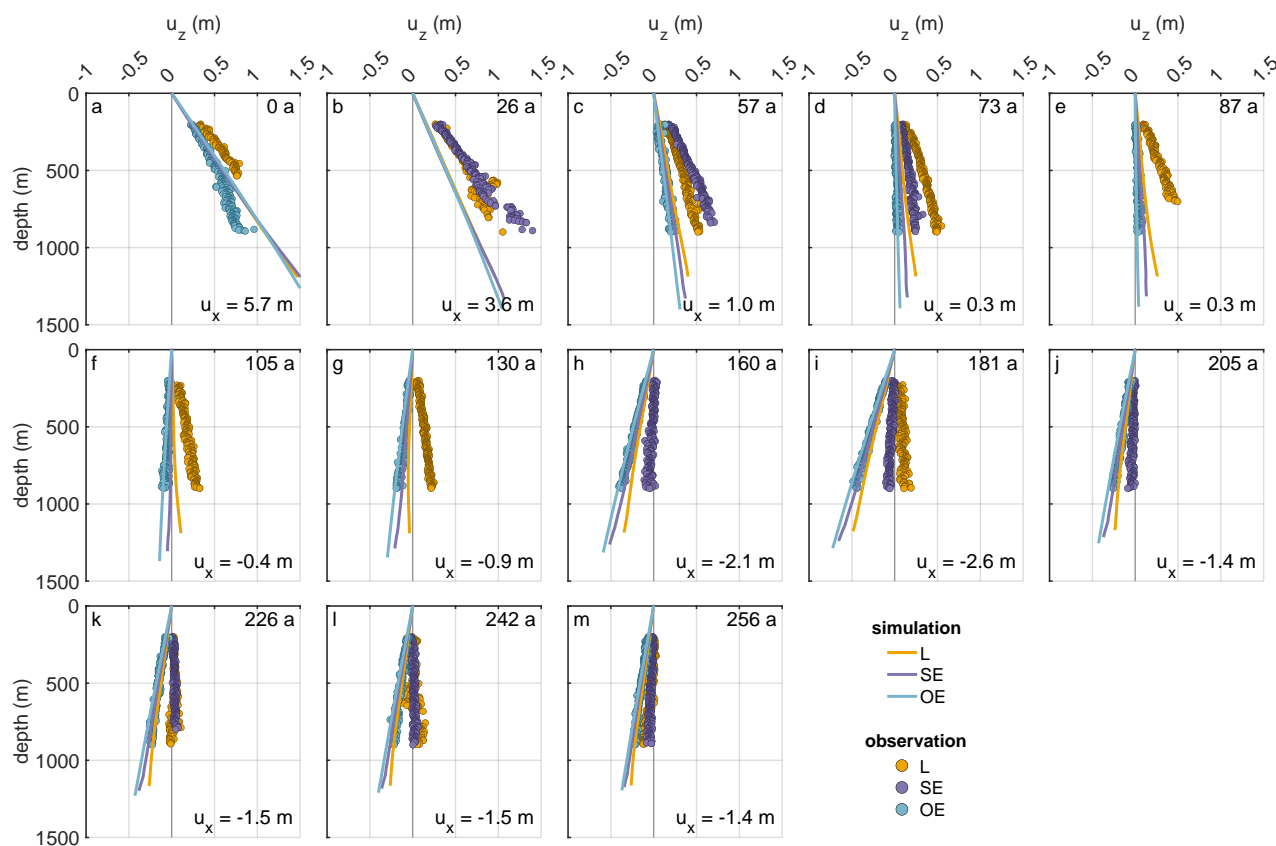
Figure B5. First experiment: comparison of displacements (u_z) derived from pRES measurements (dots) and from the simulations (lines). The different panels show the displacement for $\Delta t = 1\,\mathrm{a}$ allocated to the year of the model (number in upper right corner). The numbers in the lower right corners give horizontal displacement u_x derived from ε_{zz} of the pRES measurements outside the channel (OE) with positive values representing compression and negative values extension.
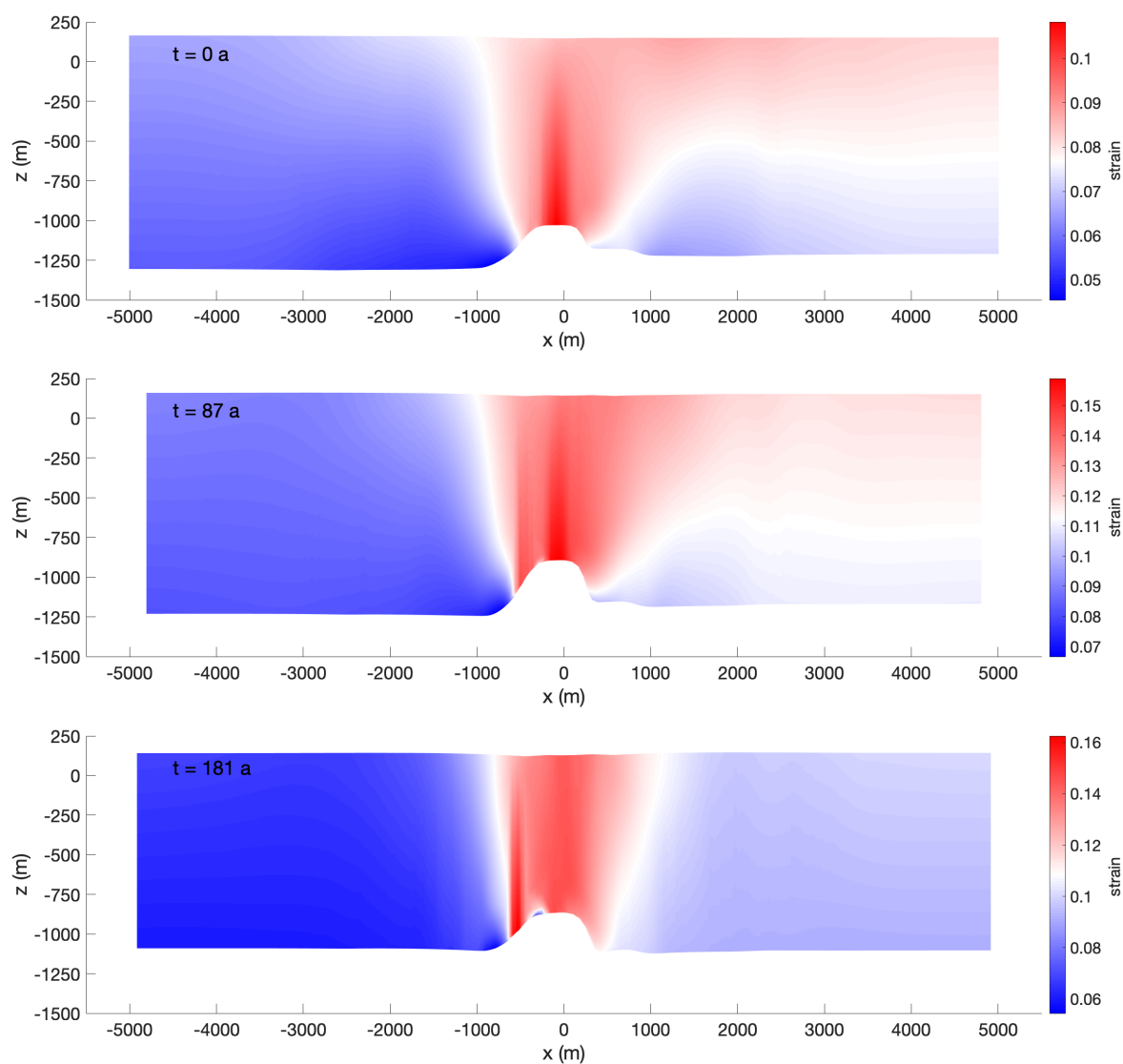
Figure B6. Simulated vertical strain of the current configuration of the second experiment using synthetic melt rates for (a) $t = 0\,\text{a}$ (after the spin-up, maximum lateral compression), (b) $t = 87\,\text{a}$ (small lateral displacement), (c) $t = 181\,\text{a}$ (maximum lateral extension). The white color shows the mean strain at each point in time. Bluish colors denote a strain deviation that is smaller than the mean value, while for the reddish areas the strain is higher. The highest strain occurs inside the channel caused by the viscous flow. The geometry variation caused by the melt rate counteract this ice flow and the basal channel persists. The maximum strain value increases from a to c through an increasing simulation time.
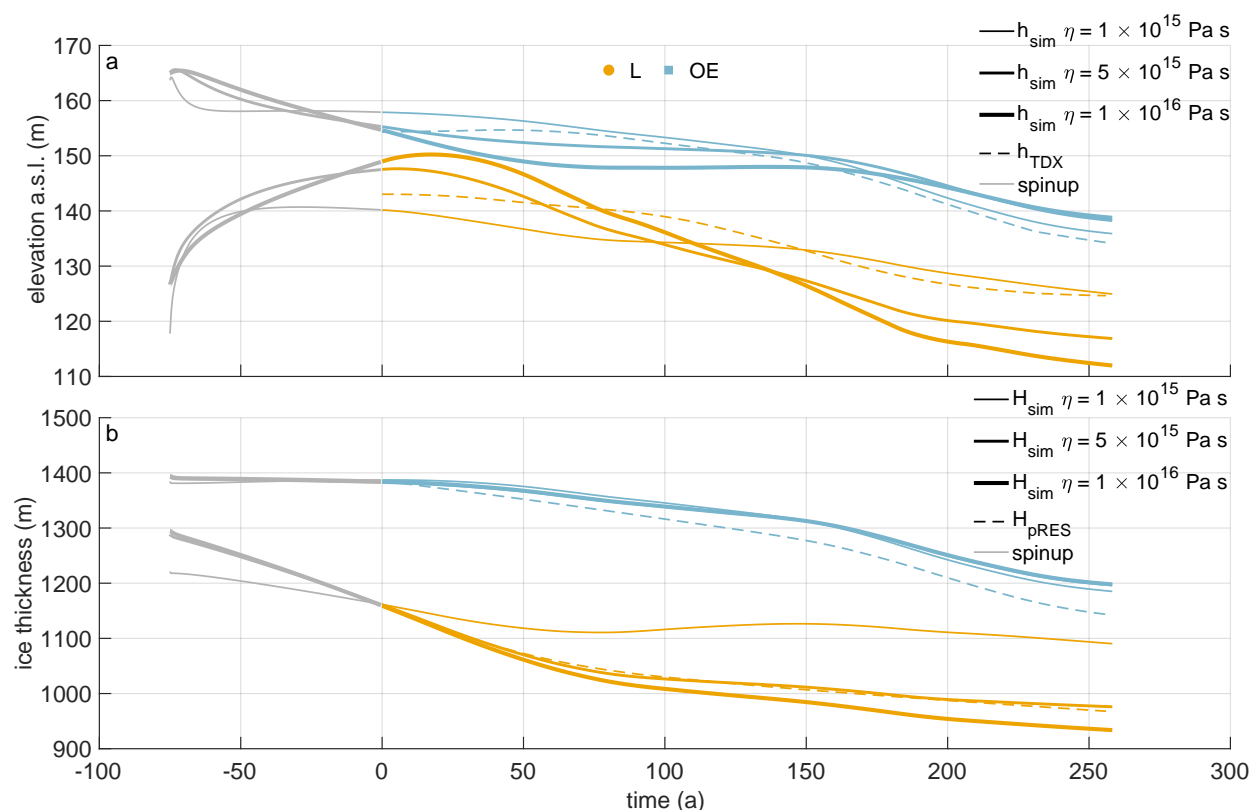
Figure B7. (a) Surface elevation above the channel (yellow) and outside the channel (blue) derived from the simulation (solid lines) and from TanDEM-X DLR (2020) (dashed lines). (b) Ice thickness above the channel (yellow) and outside the channel (blue) derived from the simulation (solid lines) and from pRES measurements (dashed lines). The thickness of the solid lines represents the different viscosities: $1 \times 10^{15}\,\mathrm{Pa\,s}$ (thin line), $5 \times 10^{15}\,\mathrm{Pa\,s}$ (medium line, same value as in the second experiment), $1 \times 10^{16}\,\mathrm{Pa\,s}$ (thick line). Gray lines represent values used in the spin-up and colored lines values used in the simulation of the evolution of the channel.

Author contributions. AH has designed the study, conducted the field study together with DS and wrote the manuscript together with OZ, JC, KWN, VH and LH. OZ processed the pRES/ApRES data and analyzed the melt rates together with AH. JC performed the viscoelastic simulations together with TS and with contributions from OZ and AH. JC, AH and OZ analyzed the results together with RM. VH and OZ processed the GPS data. LH and MW performed the inverse modeling. CH performed the seismic measurements and supported the discussions. NN calculated the TDX-DEM. KWN supported the field study and contributed to melt rate analysis and its discussion together with HFJC. All authors helped to improve writing.

525

Competing interests. The authors declare that they have no conflict of interest.

Acknowledgements. This work was funded by the AWI strategy fund project FISP. We acknowledge the support of BAS for the field campaign, in particular the support of the Graham Niven and Bradley Morell, who have been field assistants in the two expeditions. L.H. is funded through the Helmholtz School for Marine Data Science (MarDATA), Grant No. HIDSS-0005. Support for this work came from the UK Natural Environment Research Council large grant "Ice shelves in a warming world: Filchner Ice Shelf System" (NE/L013770/1).

530

References

Alley, K. E., Scambos, T. A., Alley, R. B., and Holschuh, N.: Troughs developed in ice-stream shear margins precondition ice shelves for ocean-driven breakup, Science Advances, 5, eaax2215, https://doi.org/10.1126/sciadv.aax2215, 2019.

535 Blatter, H.: Velocity and stress fields in grounded glaciers: a simple algorithm for including deviatoric stress gradients, Journal of Glaciology, 41, 333–344, https://doi.org/10.3189/S002214300001621X, 1995.

Brennan, P. V., Lok, L. B., Nicholls, K., and Corr, H.: Phase-sensitive FMCW radar system for high-precision Antarctic ice shelf profile monitoring, IET Radar, Sonar & Navigation, 8, 776–786, https://doi.org/10.1049/iet-rsn.2013.0053, 2014.

Christmann, J., Plate, C., Müller, R., and Humbert, A.: Viscous and viscoelastic stress states at the calving front of Antarctic ice shelves,
540 Annals of Glaciology, 57, 10–18, https://doi.org/10.1017/aog.2016.18, 2016.

Christmann, J., Müller, R., and Humbert, A.: On nonlinear strain theory for a viscoelastic material model and its implications for calving of ice shelves, Journal of Glaciology, 65, 212–224, https://doi.org/10.1017/jog.2018.107, 2019.

Christmann, J., Helm, V., Khan, S. A., Kleiner, T., Müller, R., Morlighem, M., Neckel, N., Rückamp, M., Steinhage, D., Zeising, O., and Humbert, A.: Elastic deformation plays a non-negligible role in Greenland's outlet glacier flow, Communications Earth & Environment,
545 2, 232, https://doi.org/10.1038/s43247-021-00296-3, 2021.

Corr, H. F., Jenkins, A., Nicholls, K. W., and Doake, C.: Precise measurement of changes in ice-shelf thickness by phase-sensitive radar to determine basal melt rates, Geophysical Research Letters, 29, 73–1 73–4, https://doi.org/10.1029/2001GL014618, 2002.

Dinniman, M. S., Asay-Davis, X. S., Galton-Fenzi, B. K., Holland, P. R., Jenkins, A., and Timmermann, R.: Modeling Ice Shelf/Ocean Interaction in Antarctica: A Review, Oceanography, 29, 144–153, https://doi.org/10.5670/oceanog.2016.106, 2016.

550 DLR: TanDEM-X - PolarDEM - Antarctica, 90m, https://doi.org/10.15489/9jhr18jepi65, 2020.

Dow, C. F., Lee, W. S., Greenbaum, J. S., Greene, C. A., Blankenship, D. D., Poinar, K., Forrest, A. L., Young, D. A., and Zappa, C. J.: Basal channels drive active surface hydrology and transverse ice shelf fracture, Science Advances, 4, https://doi.org/10.1126/sciadv.aao7212, 2018.

Drews, R.: Evolution of ice-shelf channels in Antarctic ice shelves, The Cryosphere, 9, 1169–1181, https://doi.org/10.5194/tc-9-1169-2015,
555 2015.

Drews, R., Pattyn, F., Hewitt, I. J., Ng, F. S. L., Berger, S., Matsuoka, K., Helm, V., Bergeot, N., Favier, L., and Neckel, N.: Actively evolving subglacial conduits and eskers initiate ice shelf channels at an Antarctic grounding line, Nature Communications, 8, 15 228, https://doi.org/10.1038/ncomms15228, 2017.

Dutrieux, P., Stewart, C., Jenkins, A., Nicholls, K. W., Corr, H. F., Rignot, E., and Steffen, K.: Basal terraces on melting ice shelves,
560 Geophysical Research Letters, 41, 5506–5513, https://doi.org/10.1002/2014GL060618, 2014.

Eisen, O., Winter, A., Steinhage, D., Kleiner, T., and Humbert, A.: Basal roughness of the East Antarctic Ice Sheet in relation to flow speed and basal thermal state, Annals of Glaciology, 61, 162–175, https://doi.org/10.1017/aog.2020.47, 2020.

Foerste, C., Bruinsma, S., Abrykosov, O., Lemoine, J.-M., Marty, J. C., Flechtner, F., Balmino, G., Barthelmes, F., and Biancale, R.: EIGEN-6C4 The latest combined global gravity field model including GOCE data up to degree and order 2190 of GFZ Potsdam and GRGS
565 Toulouse, https://doi.org/10.5880/icgem.2015.1, 2014.

Fujita, S., Matsuoka, T., Ishida, T., Matsuoka, K., and Mae, S.: A summary of the complex dielectric permittivity of ice in the megahertz range and its applications for radar sounding of polar ice sheets, in: Physics of ice core records, pp. 185–212, Hokkaido University Press, 2000.

Galton-Fenzi, B. K., Hunter, J. R., Coleman, R., Marsland, S. J., and Warner, R. C.: Modeling the basal melting and marine ice accretion of the Amery Ice Shelf, Journal of Geophysical Research: Oceans, 117, https://doi.org/10.1029/2012JC008214, 2012.

Gladish, C. V., Holland, D. M., Holland, P. R., and Price, S. F.: Ice-shelf basal channels in a coupled ice/ocean model, Journal of Glaciology, 58, 1227–1244, https://doi.org/10.3189/2012JoG12J003, 2012.

Gudmundsson, H.: Ice-stream response to ocean tides and the form of the basal sliding law, The Cryosphere, 5 (1), 259–270, https://doi.org/10.5194/tc-5-259-2011, 2011.

Gwyther, D. E., Kusahara, K., Asay-Davis, X. S., Dinniman, M. S., and Galton-Fenzi, B. K.: Vertical processes and resolution impact ice shelf basal melting: A multi-model study, Ocean Modelling, 147, 101 569, https://doi.org/10.1016/j.ocemod.2020.101569, 2020.

Haupt, P.: Continuum Mechanics and Theory of Materials, Springer, Berlin, https://doi.org/10.1007/978-3-662-04775-0, 2002.

Helm, V., Humbert, A., and Miller, H.: Elevation and elevation change of Greenland and Antarctica derived from CryoSat-2, The Cryosphere, 8, 1539–1559, https://doi.org/10.5194/tc-8-1539-2014, 2014.

Herron, M. M. and Langway, C. C.: Firn densification: an empirical model, Journal of Glaciology, 25, 373–385, https://doi.org/10.3189/S0022143000015239, 1980.

Hofstede, C., Beyer, S., Corr, H., Eisen, O., Hattermann, T., Helm, V., Neckel, N., Smith, E. C., Steinhage, D., Zeising, O., and Humbert, A.: Evidence for a grounding line fan at the onset of a basal channel under the ice shelf of Support Force Glacier, Antarctica, revealed by reflection seismics, The Cryosphere, 15, 1517–1535, https://doi.org/10.5194/tc-15-1517-2021, 2021a.

Hofstede, C., Beyer, S., Corr, H. F. J., Eisen, O., Hattermann, T., Helm, V., Neckel, N., Smith, E. C., Steinhage, D., Zeising, O., and Humbert, A.: Seismic reflection data of a basal channel and ocean cavity at the ice shelf-grounding line area of Support Force Glacier, Filchner Ice Shelf, Antarctica, https://doi.org/10.1594/PANGAEA.932278, 2021b.

Holland, P. R. and Kwok, R.: Wind-driven trends in Antarctic sea-ice drift, Nature Geoscience, 5, 872–875, https://doi.org/10.1038/ngeo1627, 2012.

Howat, I., Morin, P., Porter, C., and Noh, M.-J.: The Reference Elevation Model of Antarctica, https://doi.org/10.7910/DVN/SAIK8B, 2018.

Howat, I., Porter, C., Smith, B. E., Noh, M.-J., and Morin, P.: The Reference Elevation Model of Antarctica, The Cryosphere, 13, 665–674, https://doi.org/10.5194/tc-13-665-2019, 2019.

Humbert, A., Steinhage, D., Helm, V., Hoerz, S., Berendt, J., Leipprand, E., Christmann, J., Plate, C., and Müller, R.: On the link between surface and basal structures of the Jelbart Ice Shelf, Antarctica, Journal of Glaciology, 61, 975–986, https://doi.org/10.3189/2015JoG15J023, 2015.

Humbert, A., Steinhage, D., Helm, V., Beyer, S., and Kleiner, T.: Missing evidence of widespread subglacial lakes at Recovery Glacier, Antarctica, Journal of Geophysical Research: Earth Surface, 123, 2802–2826, https://doi.org/10.1029/2017JF004591, 2018.

Jenkins, A., Corr, H. F., Nicholls, K. W., Stewart, C. L., and Doake, C. S.: Interactions between ice and ocean observed with phase-sensitive radar near an Antarctic ice-shelf grounding line, Journal of Glaciology, 52, 325–346, https://doi.org/10.3189/172756506781828502, 2006.

Jeofry, H., Ross, N., Le Brocq, A., Graham, A. G. C., Li, J., Gogineni, P., Morlighem, M., Jordan, T., and Siegert, M. J.: Hard rock landforms generate 130 km ice shelf channels through water focusing in basal corrugations, Nature Communications, 8, 4576, https://doi.org/10.1038/s41467-018-06679-z, 2018.

Jourdain, N. C., Mathiot, P., Merino, N., Durand, G., Le Sommer, J., Spence, P., Dutrieux, P., and Madec, G.: Ocean circulation and sea-ice thinning induced by melting ice shelves in the Amundsen Sea, Journal of Geophysical Research: Oceans, 122, 2550–2573, https://doi.org/10.1002/2016JC012509, 2017.

Kovacs, A., Gow, A. J., and Morey, R. M.: The in-situ dielectric constant of polar firn revisited, Cold Regions Science and Technology, 23, 245 – 256, https://doi.org/10.1016/0165-232X(94)00016-Q, 1995.

Langley, K., von Deschwanden, A., Kohler, J., Sinisalo, A., Matsuoka, K., Hattermann, T., Humbert, A., Nøst, O., and Isaksson, E.: Complex network of channels beneath an Antarctic ice shelf, Geophysical Research Letters, 41, 1209–1215, https://doi.org/10.1002/2013GL058947, 2014.

Larour, E., Seroussi, H., Morlighem, M., and Rignot, E.: Continental scale, high order, high spatial resolution, ice sheet modeling using the Ice Sheet System Model (ISSM), Journal of Geophysical Research: Earth Surface, 117, F01 022, https://doi.org/10.1029/2011JF002140, 2012.

Le Brocq, A. M., Ross, N., Griggs, J. A., Bingham, R. G., Corr, H. F., Ferraccioli, F., Jenkins, A., Jordan, T. A., Payne, A. J., Rippin, D. M., et al.: Evidence from ice shelves for channelized meltwater flow beneath the Antarctic Ice Sheet, Nature Geoscience, 6, 945, https://doi.org/10.1038/ngeo1977, 2013.

Marsh, O. J., Fricker, H. A., Siegfried, M. R., Christianson, K., Nicholls, K. W., Corr, H. F., and Catania, G.: High basal melting forming a channel at the grounding line of Ross Ice Shelf, Antarctica, Geophysical Research Letters, 43, 250–255, https://doi.org/10.1002/2015GL066612, 2016.

Martos, Y. M., Catalán, M., Jordan, T. A., Golynsky, A., Golynsky, D., Eagles, G., and Vaughan, D. G.: Heat Flux Distribution of Antarctica Unveiled, Geophysical Research Letters, 44, 11,417–11,426, https://doi.org/10.1002/2017GL075609, 2017.

Millgate, T., Holland, P. R., Jenkins, A., and Johnson, H. L.: The effect of basal channels on oceanic ice-shelf melting, Journal of Geophysical Research: Oceans, 118, 6951–6964, https://doi.org/10.1002/2013JC009402, 2013.

Morlighem, M.: MEaSUREs BedMachine Antarctica, Version 2. Boulder, Colorado USA. NASA National Snow and Ice Data Center Distributed Active Archive Center, Accessed 12 April 2021, https://doi.org/10.5067/E1QL9HFQ7A8M, 2020.

Morlighem, M., Rignot, E., Binder, T., Blankenship, D., Drews, R., Eagles, G., Eisen, O., Ferraccioli, F., Forsberg, R., Fretwell, P., Goel, V., Greenbaum, J. S., Gudmundsson, H., Guo, J., Helm, V., Hofstede, C., Howat, I., Humbert, A., Jokat, W., Karlsson, N. B., Lee, W. S., Matsuoka, K., Millan, R., Mouginot, J., Paden, J., Pattyn, F., Roberts, J., Rosier, S., Ruppel, A., Seroussi, H., Smith, E. C., Steinhage, D., Sun, B., Broeke, M. R. v. d., Ommen, T. D. v., Wessem, M. v., and Young, D. A.: Deep glacial troughs and stabilizing ridges unveiled beneath the margins of the Antarctic ice sheet, Nature Geoscience, 13, 132–137, https://doi.org/10.1038/s41561-019-0510-8, 2020.

Mouginot, J., Rignot, E., and Scheuchl, B.: MEaSUREs Phase-Based Antarctica Ice Velocity Map, Version 1. Boulder, Colorado USA. NASA National Snow and Ice Data Center Distributed Active Archive Center, Accessed 13 April 2021, https://doi.org/10.5067/PZ3NJ5RXRH10, 2019a.

Mouginot, J., Rignot, E., and Scheuchl, B.: Continent-Wide, Interferometric SAR Phase, Mapping of Antarctic Ice Velocity, Geophysical Research Letters, 46, 9710–9718, https://doi.org/10.1029/2019GL083826, 2019b.

Naughten, K. A., De Rydt, J., Rosier, S. H. R., Jenkins, A., Holland, P. R., and Ridley, J. K.: Two-timescale response of a large Antarctic ice shelf to climate change, Nature Communications, 12, 1991, https://doi.org/10.1038/s41467-021-22259-0, 2021.

Nicholls, K. W.: Predicted reduction in basal melt rates of an Antarctic ice shelf in a warmer climate, Nature, 388, 460–462, https://doi.org/10.1038/41302, 1997.

Nicholls, K. W.: The study of ice shelf-ocean interaction—techniques and recent results, Advances in Polar Science, 3, 222–230, https://doi.org/10.13679/j.advps.2018.3.00222, 2018.

Nicholls, K. W., Corr, H. F., Stewart, C. L., Lok, L. B., Brennan, P. V., and Vaughan, D. G.: A ground-based radar for measuring vertical strain rates and time-varying basal melt rates in ice sheets and shelves, Journal of Glaciology, 61, 1079–1087, https://doi.org/10.3189/2015JoG15J073, 2015.

645 Pattyn, F.: A new three-dimensional higher-order thermomechanical ice sheet model: Basic sensitivity, ice stream development, and ice flow across subglacial lakes, J. Geophys. Res. Solid Earth, 108, https://doi.org/10.1029/2002JB002329, 2003.

Reeh, N., Mayer, C., Olesen, O. B., Christensen, E. L., and Thomsen, H. H.: Tidal movement of Nioghalvfjerdsfjorden glacier, northeast Greenland: observations and modelling, Annals of Glaciology, 31, 111–117, https://doi.org/10.3189/172756400781820408, 2000.

Rignot, E. and Steffen, K.: Channelized bottom melting and stability of floating ice shelves, Geophysical Research Letters, 35,
650 https://doi.org/10.1029/2007GL031765, 2008.

Rizzoli, P., Martone, M., Gonzalez, C., Wecklich, C., Borla Tridon, D., Bräutigam, B., Bachmann, M., Schulze, D., Fritz, T., Huber, M., Wessel, B., Krieger, G., Zink, M., and Moreira, A.: Generation and performance assessment of the global TanDEM-X digital elevation model, ISPRS Journal of Photogrammetry and Remote Sensing, 132, 119–139, https://doi.org/10.1016/j.isprsjprs.2017.08.008, 2017.

Schultz, T.: Viskoelastische Modellierung der Dynamik eines Gletschers als Antwort auf basales Schmelzen und die Oberflächenmassenbi-
655 lanz, Master thesis, 2017.

Sergienko, O.: Basal channels on ice shelves, Journal of Geophysical Research: Earth Surface, 118, 1342–1355, https://doi.org/10.1002/jgrf.20105, 2013.

Seroussi, H., Nakayama, Y., Larour, E., Menemenlis, D., Morlighem, M., Rignot, E., and Khazendar, A.: Continued retreat of Thwaites Glacier, West Antarctica, controlled by bed topography and ocean circulation, Geophysical Research Letters, 44, 6191–6199,
660 https://doi.org/10.1002/2017GL072910, 2017.

Smith, B. E., Fricker, H. A., Joughin, I. R., and Tulaczyk, S.: An inventory of active subglacial lakes in Antarctica detected by ICESat (2003–2008), Journal of Glaciology, 55, 573–595, https://doi.org/10.3189/002214309789470879, 2009.

Stanton, T., Shaw, W., Truffer, M., Corr, H., Peters, L., Riverman, K., Bindschadler, R., Holland, D., and Anandakrishnan, S.: Channelized ice melting in the ocean boundary layer beneath Pine Island Glacier, Antarctica, Science, 341, 1236–1239,
665 https://doi.org/10.1126/science.1239373, 2013.

Stewart, C. L., Christoffersen, P., Nicholls, K. W., Williams, M. J., and Dowdeswell, J. A.: Basal melting of Ross Ice Shelf from solar heat absorption in an ice-front polynya, Nature Geoscience, 12, 435, https://doi.org/10.1038/s41561-019-0356-0, 2019.

Timmermann, R. and Hellmer, H.: Southern Ocean warming and increased ice shelf basal melting in the twenty-first and twenty-second centuries based on coupled ice-ocean finite-element modelling, Ocean Dynamics, 63, https://doi.org/10.1007/s10236-013-0642-0, 2013.

670 van Wessem, J., Reijmer, C., Morlighem, M., Mouginot, J., Rignot, E., Medley, B., Joughin, I., Wouters, B., Depoorter, M., Bamber, J., et al.: Improved representation of East Antarctic surface mass balance in a regional atmospheric climate model, Journal of Glaciology, 60, 761–770, https://doi.org/10.3189/2014JoG14J051, 2014.

Vaňková, I., Nicholls, K. W., Corr, H. F., Makinson, K., and Brennan, P. V.: Observations of tidal melt and vertical strain at the Filchner-Ronne Ice Shelf, Antarctica, Journal of Geophysical Research: Earth Surface, 125, e2019JF005 280, https://doi.org/10.1029/2019JF005280,
675 2020.

Vaňková, I., Nicholls, K. W., and Corr, H. F. J.: The Nature of Ice Intermittently Accreted at the Base of Ronne Ice Shelf, Antarctica, Assessed Using Phase-Sensitive Radar, Journal of Geophysical Research: Oceans, 126, e2021JC017 290, https://doi.org/10.1029/2021JC017290, 2021.

Vaughan, D. G., Corr, H. F., Bindschadler, R. A., Dutrieux, P., Gudmundsson, G. H., Jenkins, A., Newman, T., Vornberger, P., and Wingham,
    D. J.: Subglacial melt channels and fracture in the floating part of Pine Island Glacier, Antarctica, Journal of Geophysical Research: Earth
    Surface, 117, https://doi.org/10.1029/2012JF002360, 2012.

Washam, P., Nicholls, K. W., Münchow, A., and Padman, L.: Summer surface melt thins Petermann Gletscher Ice Shelf by enhancing
    channelized basal melt, Journal of Glaciology, 65, 662–674, https://doi.org/10.1017/jog.2019.43, 2019.

Wearing, M. G., Stevens, L. A., Dutrieux, P., and Kingslake, J.: Ice-Shelf Basal Melt Channels Stabilized by Secondary Flow, Geophysical
    Research Letters, 48, e2021GL094 872, https://doi.org/10.1029/2021GL094872, 2021.

Zeising, O. and Humbert, A.: Indication of high basal melting at the EastGRIP drill site on the Northeast Greenland Ice Stream, The
    Cryosphere, 15, 3119–3128, https://doi.org/10.5194/tc-15-3119-2021, 2021.

Zeising, O., Steinhage, D., Nicholls, K. W., Corr, H. F. J., Stewart, C. L., and Humbert, A.: Basal melt of the southern Filchner Ice Shelf,
    Antarctica, The Cryosphere Discussions [preprint], pp. 1–19, https://doi.org/10.5194/tc-2021-230, 2021.